Acta Pharmaceutica Sinica B 2023;13(3):1071−1092

Chinese Pharmaceutical Association
Institute of Materia Medica, Chinese Academy of Medical Sciences

Acta Pharmaceutica Sinica B

www.elsevier.com/locate/apsb
www.sciencedirect.com

ORIGINAL ARTICLE

The deubiquitinating enzyme 13 retards non-alcoholic steatohepatitis *via* blocking inactive rhomboid protein 2-dependent pathway

Minxuan Xu[a,b,c,*,†], Jun Tan[a,b,*,†], Liancai Zhu[c,†], Chenxu Ge[a,b,c,†], Wei Dong[d,†], Xianling Dai[a,c], Qin Kuang[a,c], Shaoyu Zhong[a,b], Lili Lai[a,b], Chao Yi[a,b], Qiang Li[a,b], Deshuai Lou[a,b], Linfeng Hu[a,b,c], Xi Liu[a,b], Gang Kuang[a,b], Jing Luo[a,b], Jing Feng[c], Bochu Wang[c,*]

[a]*Chongqing Key Laboratory of Medicinal Resources in the Three Gorges Reservoir Region, School of Biological and Chemical Engineering, Chongqing University of Education, Chongqing 400067, China*
[b]*College of Modern Health Industry, Chongqing University of Education, Chongqing 400067, China*
[c]*Key Laboratory of Biorheological Science and Technology (Chongqing University), Ministry of Education, College of Bioengineering, Chongqing University, Chongqing 400030, China*
[d]*Shandong Cancer Hospital and Institute, Shandong First Medical University & Shandong Academy of Medical Sciences, Jinan 250117, China*

Received 8 July 2022; received in revised form 22 August 2022; accepted 26 October 2022

KEY WORDS

Usp13;
Irhom2;
NASH;
Hepatosteatosis;
Ubc13;
NAFLD;
Ubiquitination;
Liver inflammation

Abstract Nowadays potential preclinical drugs for the treatment of nonalcoholic steatohepatitis (NASH) have failed to achieve expected therapeutic efficacy because the pathogenic mechanisms are underestimated. Inactive rhomboid protein 2 (IRHOM2), a promising target for treatment of inflammation-related diseases, contributes to deregulated hepatocyte metabolism-associated nonalcoholic steatohepatitis (NASH) progression. However, the molecular mechanism underlying Irhom2 regulation is still not completely understood. In this work, we identify the ubiquitin-specific protease 13 (USP13) as a critical and novel endogenous blocker of IRHOM2, and we also indicate that USP13 is an IRHOM2-interacting protein that catalyzes deubiquitination of Irhom2 in hepatocytes. Hepatocyte-specific loss of the *Usp13* disrupts liver metabolic homeostasis, followed by glycometabolic disorder, lipid deposition, increased inflammation, and markedly promotes NASH development. Conversely, transgenic mice with *Usp13* overexpression, lentivirus (LV)- or adeno-associated virus (AAV)-driven *Usp13* gene therapeutics

*Corresponding authors.
E-mail addresses: minxuanxu@foxmail.com (Minxuan Xu), tanjun@cque.edu.cn (Jun Tan), wangbc2000@126.com (Bochu Wang).
[†]These authors made equal contributions to this work.
Peer review under the responsibility of Chinese Pharmaceutical Association and Institute of Materia Medica, Chinese Academy of Medical Sciences.

https://doi.org/10.1016/j.apsb.2022.12.006
2211-3835 © 2023 Chinese Pharmaceutical Association and Institute of Materia Medica, Chinese Academy of Medical Sciences. Production and hosting by Elsevier B.V. This is an open access article under the CC BY-NC-ND license (http://creativecommons.org/licenses/by-nc-nd/4.0/).

mitigates NASH in 3 models of rodent. Mechanistically, in response to metabolic stresses, USP13 directly interacts with IRHOM2 and removes its K63-linked ubiquitination induced by ubiquitin-conjugating enzyme E2N (UBC13), a ubiquitin E2 conjugating enzyme, and thus prevents its activation of downstream cascade pathway. USP13 is a potential treatment target for NASH therapy by targeting the Irhom2 signaling pathway.

© 2023 Chinese Pharmaceutical Association and Institute of Materia Medica, Chinese Academy of Medical Sciences. Production and hosting by Elsevier B.V. This is an open access article under the CC BY-NC-ND license (http://creativecommons.org/licenses/by-nc-nd/4.0/).

1. Introduction

The rising prevalence of obesity and its related complications has been regarded as a global pandemic in many countries[1]. Continued long-term intake of over-nutrition diets elevate the risk of chronic metabolism syndrome (MetS), *e.g.*, coronary heart disease, hypertension, type II diabetes (T2D), severe cardio-cerebrovascular disease, and nonalcoholic fatty liver disease (NAFLD)[2−4]. Of note, the prevalence of obesity-related comorbidities such as NAFLD, which affects 35% of adults and about 70% of people with obesity and diabetes, is also increasing[2,5]. The severity of NAFLD changed from hepatosteatosis to vicious transformation of hepatocytes and necroinflammatory alterations characterized by nonalcoholic steatohepatitis (NASH), suggesting that patients had higher hepatic fibrosis and hepatocellular carcinoma (HCC) risk and are more susceptible to these pathological progressions[6,7]. Indeed, NAFLD, as a heterogeneous disease with complex physiopathology and molecular signaling pathways, may not be share the same pathological process in each individual patient[8]. As it is, currently, there are no approved and proven perfectly valid pharmaceutic therapeutics approaches for NASH treatment all over the world, and the efforts to alleviate the associated complications from the disease have not quite lived up to expectations. Recently, it is even more regrettable that a series of potential drugs for the treatment of NASH (*e.g.*, selonsertib, elafibranor and GR-MD-02) have failed to achieve expected therapeutic efficacy because they did not meet the expected clinical endpoint[9−11]. The failure of these promising clinical treatment drugs further proved that the pathological process of NASH involving a complicated molecular mechanism and may also track with many physiological and metabolic processes. Therefore, further thorough pharmacopathological studies demand to determine the pivotal molecular modulators accurately and comprehensively for the occurrence and progression of NASH, so as to develop more effective treatment options. Inactive rhomboid protein 2 (also named as Rhbdf2, hereunder named as Irhom2), an inactive rhomboid protease, has been identified as a crucial and positive regulator of inflammation-associated diseases *e.g.*, NAFLD, obesity, arthrophlogosis, renal injury, atherosis, and fibration[12−15]. Our previous reports and recent studies also determined that Irhom2 recruited transforming growth factor β activated kinase 1 (MAP3K7) to markedly elevate its levels of phosphorylation and increase downstream pro-inflammatory signaling cascade[12,13,16,17]. However, whether there are potential factors that regulate Irhom2-mediated NASH pathogenesis is unclear. Thus, an urgent study is vital to determine the controlling signaling leading to Irhom2−MAP3K7 inactivation or block of NASH progression.

Deubiquitinating enzyme 13 (IsoT-3, hereunder named as USP13), an important member of the deubiquitinating-enzymes family (DUBs), has been recognized as a “multi-faced” factor in innate immune responses by regulating the potential target protein ubiquitination modification to mediate signal transduction[18,19]. Previous report have revealed that p53, an important tumor suppressor, is associated with USP13 in tumorigenesis by deubiquitinating modification[20]. Also, USP13 has been confirmed to deubiquitinate, maintain Stat1 signaling and then provoke interferon (IFN) signaling cascade[21]. Recently, USP13 also has been reported to be a key regulator in STING-mediated antiviral responses. USP13 is able to directly interact with stimulator of IFN response cGAMP inter-actor 1 (STING) by suppressing the recruitment of TBK1 *via* removing K27- and K33-linked, but not K63-linked polyubiquitination modification of STING[22]. Given the close correlation between USP13 and STING, thus we suspect that Irhom2 may be associated with the governance of USP13 under the pathological circumstances. Interestingly, USP13 also has been determined to be a regulator in DNA repair. USP13 promoted RAP80−BRCA1 complex formation and USP13 participated in DNA repair progression by deubiquitinating the K63-linked polyubiquitination of RAP80 *in vivo* and *in vitro*[23]. These seemingly controversial findings showed that USP13 actually performed unique biological function in different physiological processes.

In this current study, we demonstrated that USP13 activity is notably restrained in livers of rodent NASH models. Of note, we observed a marked downregulation of USP13 in livers, which is negatively correlated with the expression of NASH markers in human patients. In a series of mice models with NASH phenotype, hepatocyte-specific deficiency of USP13 dramatically potentiated hepatosteatosis, hepatic inflammation, and hepatofibrosis, whereas USP13 overexpression in hepatocytes efficiently suppressed NASH diet-induced steatohepatitis. Mechanistically, we further determined that USP13 directly interacts with IRHOM2 and removes its K63-linked ubiquitination induced by ubiquitin-conjugating enzyme E2N (UBC13), a ubiquitin E2 conjugating enzyme, and thus prevents its activation of downstream cascade. These findings demonstrate a novel mechanism for the USP13-regulated IRHOM2 high expression in NASH progression, and provide a potential and promising molecular target for more specific therapy of steatohepatitis in future targeted drug development.

2. Materials and methods

2.1. Research consent and ethical statement

The purpose of the current work was to (1) identify the correlation of USP13 expression in livers with severity of NASH in patients, (2) identify what role USP13 activity alteration plays in NASH-

related lipid deposition, inflammation and fibrosis progress by combining a series of dietary rodent models of NASH with *Usp13* loss (Hep^{Usp13}KO) and gain-of-function (Hep^{Usp13}OE, Hep$^{Usp13\text{-}GOF}$ and Hep$^{Usp13(\triangle UBA)}$GOF) transgenic expression mice, and (3) determine the USP13-regulated downstream signaling cascade in suppression of NASH pathogenesis by a series of adeno-associated virus (AAV)-mediated knockdown method *in vivo* and adenovirus (Ad)-mediated *in vitro* experiments. The whole experimental protocols regarding animals used in this study were permitted by the *Guide for the Care & Use of Laboratory Animals* (8th edition NIH, in Chinese) and permitted by the *Institutional Animal Use & Care Committee (IACUC)* in Chongqing University of Education (20190012CQUE). The approaches and procedures involved in current work were used in line with the *Regulations of the People's Republic of China on the Administration of Experimental Animals (Revised & Exposure Draft)*, issued by the *Ministry of Science and Technology (MOST) of the People's Republic of China* (http://www.most.gov.cn).

2.2. Liver samples of human donors

Human donors' liver specimens were harvested from adult donors with NAFLD who underwent biopsy tissue samples or liver transplantation samples. The relevant non-steatotic liver tissues were obtained from donors who were not eligible for liver transplantation for non-liver reasons. Non-steatosis samples ($n = 16$), simple steatosis samples ($n = 17$), and NASH phenotype liver samples ($n = 16$) were obtained and included in this study. Of note, steatotic liver samples from patients with any of the following conditions were excluded from the study: excessive drinking (alcohol $>$ 70 g for female or alcohol $>$ 140 g for male, per week), viral infection or drug abuse (including hepatitis B and C virus infection). Also, prior to this study, the samples of non-steatosis and simple steatosis in this cohort were collected from patients without taking statins or insulin. The NASH phenotype liver samples ($n = 16$) in this cohort were from patients who had taken pioglitazone (15−30 mg/day) for no more than 24 months. Liver sample donors and their families agreed and signed written informed consent. Physiological characteristics of patients and hepatic injury-related serology are shown in Supporting Information Table S1. All protocols involving human donors in this work were grounded on *the Ethical Principles for Medical Research Involving Human Subjects, Declaration of Helsink (*64th WMA *general assembly)*, and totally approved by the *Academic Committee of Experimental Animal Ethics, Use & Care Union* in Chongqing University of Education and other participating units.

2.3. Mouse strains

To obtain practicable mice with a conditional deletion of *Usp13*, the *Usp13$^{flox/flox}$* mice based on C57BL/6 strain were created by Clustered Regularly Interspersed Short Palindromic Repeats-CRISPR-associated protein 9 (CRISPR-Cas9) genetic engineering editing system. The exon 5 of *Usp13* was targeted as conditional deletion sites to perform conditional knockout. In short, the targeted exons of *Usp13* were flanked by 2 sites of *loxP*, and thus 2 single guide RNAs, guide RNA1 and guide RNA2, targeting *Usp13* introns were demarcated. The packaged plasmids containing 2 *loxP* sites-flanked *Usp13* exons and the following 2 homology arms were regarded as corresponding template. The targeting vector, guide RNA1 and guide RNA2, and together with Cas9 were coinjected into zygotes for conditional deletion mice establishment. The achieved pups, which had targeted exons flanked by 2 *loxP* sites on 1 allele, were subjected to produce *Usp13$^{flox/flox}$* mice. Hepatocyte-specific *Usp13* ablation (Hep^{Usp13}KO) offspring were generated by crossing *Usp13$^{flox/flox}$* offspring with albumin-cre tool transgenic mice (Alb-Cre) (Cyagen Biosciences, Guangzhou, China). *Usp13$^{flox/flox}$* (Flox) mouse littermates were regarded as corresponding comparison controls for the procured Hep^{Usp13}KO mice.

To obtain mice with conditional overexpression of *Usp13*, the Rosa^{Usp13} mice ground on C57BL/6 strain were constructed by *Usp13* conditional knockin at the mouse locus of *Rosaβgeo2*6 by CRISPR-Cas9 genetic engineering editing system. Briefly, the designed cassette of *Rosaβgeo26*-(pCAG)-*loxp*-STOP-*loxp*-m*Usp13*-pA box was inserted into 1st intron of *Rosaβgeo26*. Subsequently, the targeting vector, guide RNA, and Cas9 were coinjected into spermatovums for Rosa^{Usp13} mouse establishment. In the indicated experiments, the conditional overexpression of *Usp13* in hepatocytes (Hep^{Usp13}OE) were triggered by injection of adeno-associated virus serotype-8 (AAV8)-thyroxine-binding globulin promoter (TBG)-recombinase Cre vector (AAV8-TBG-Cre) *via* intravenous injection and then determined by immunoblotting assay. Rosa^{Usp13} littermates with AAV-blank injection were used as corresponding controls for the procured Hep^{Usp13}OE mice.

To perform practicable mice with a conditional deletion of *Irhom2* (Hep^{Irhom2}KO), the *Irhom2$^{flox/flox}$* mice ground on C57BL/6 strain were created by CRISPR-Cas9 genetic engineering editing system. The exon 4th of *Irhom2* was targeted as conditional deletion sites to perform conditional knockout. Briefly, the targeted *Irhom2* exons were sided by 2 *loxP* loca, and thus 2 single guide RNAs, guide RNA1 and guide RNA2, targeting *Irhom2* introns were demarcated. The packaged plasmids containing *Irhom2* exons flanked by two *loxP* sites and the two homology arms were used as the template. The targeting plasmids, guide RNA1 and guide RNA2, and together with Cas9 were coinjected into zygotes for conditional deficient-mice establishment. The achieved pups, which had targeted exons flanked by 2 sites of *loxP* on 1 allele, were subjected to produce *Irhom2$^{flox/flox}$* mice. Hepatocyte-specific *Irhom2* ablation (Hep^{Irhom2}KO) mice were generated by crossing *Irhom2$^{flox/flox}$* mice with albumin-cre tool transgenic mice (Alb-Cre) (Cyagen Biosciences, Suzhou, China). *Irhom2$^{flox/flox}$* (Flox) mouse littermates were regarded as comparison controls for the procured Hep^{Irhom2}KO mice. The hepatocyte-specific *Usp13* & *Irhom2* dual-deficiency (Hep$^{Usp13\text{-}Irhom2}$DKO) mice were produced by mating *Usp13$^{flox/flox}$* mice with Hep^{Irhom2}KO mice. The obtained offspring without USP13 and IRHOM2 protein expression were identified and selected by western blotting assay and used for further indicated experiments. Besides, wild-type C57BL/6N strain mice (WT, male, 6−8-week-old) used in this work were purchased from SiPeiFu SPF (Beijing) Biotechnology Co., Ltd. (Beijing, China).

2.4. Nonalcoholic steatohepatitis (NASH) animal model

Three different NASH models in mice were constructed and used in the current study for the corresponding experiments. (i) High fat plus high cholesterol diet (HFHC)-mediated NASH model. A mice model with NASH phenotype was generated by feeding the mice a HFHC fodder (HFHC) (42% saturated-fat, 14% protein, 44% carbohydrates and 0.2% cholesterol *w*/*w*) for 24 weeks[24,25]. The experimental mice were treated with a standard normal chow diet (NCD) (Cat.: D12450J; Research Diets, USA) for consecutive 24

weeks to be regarded as corresponding controls for the procured HFHC model. (ii) Western-type diet plus 15% fructose (*w/v*)-drinking water (WTDF)-induced NASH model. The second mice model with NASH phenotype was obtained by feeding the corresponding mice a WTDF diet (Cat.: D12079B; Research Diets, Inc., New Brunswick, USA) supplemented with 15% *w/v* fructose (Cat.: 630030391, Sinopharm Chemical Reagent Co., Ltd., China)-drinking water (Watsons) for 24 weeks[24,25]. Control mice received normal chow diet. (iii) High fat plus Met and choline dual-deficient diet (HFMCD)-induced NASH model. The third mice model with NASH phenotype was obtained by feeding the mice a HFMCD diet (HFMCD, Cat.: A06071301B, Research Diets) for 8 weeks[24,25]. Control mice received corresponding chow diet (NCD, specialty feeds).

2.5. Animal treatment and model design

Before the experiment starts, animals participating in the corresponding experiment were forced to accommodate to their living environment for 7 days. The animals were kept at a steady temperature, moisture capacity (governed by Haier central air conditioning, Cat.: RFC140MXSCVD(G), China), and aseptic conditions-controlled environment (25 °C, 55%−60%) cage with a constant and standard 12/24 h−12/24 h light/dark circle, unlimited pathogen-free-drinking water (Cat.: 10045273913156, Watsons, China) and fodder in their houses.

2.5.1. Animal study design 1st

The WT male, 6−8-week-old mice were treated with a HFHC diet for 24 weeks to mediate NASH phenotype. The other WT mice were treated with a NCD fodder for 24 weeks to be regarded as comparison controls (NCD). The *ob/ob* mice (Cat.: B6; 129S-*Lep*^{tm1Smoc}, Shanghai Model Organisms, Shanghai, China) were treated with NCD, and then regarded as another NAFLD model. After the experiment, the liver tissues were harvested from indicated mice model to examine corresponding signal indicators.

2.5.2. Animal study design 2nd

To estimate the protective effects of USP13 on HFHC diet-triggered NASH pathologies, the *ex vivo*-mediated *Usp13* gene therapeutics administration by lentivirus-packaged full-length *Usp13* cDNA sequences (LV-*Usp13*) or shRNA targeting *Usp13* (LV-sh*Usp13*) *ex vivo* transplantation was subjected to 8-weeks HFHC-fed pretreated WT mice. Corresponding *ex vivo*-mediated gene therapeutics methods were produced in accordance with our former report[24]. After that, experimental mice were fasted for unremitting 8 h, and then shifted to analysis of glucose tolerance test (GTT).

2.5.3. Animal study design 3rd

Hepatocyte-specific *Usp13* deletion (Hep^{Usp13}KO) mice were treated with HFHC or WTDF diet for 24 weeks to induce NASH phenotype, respectively. To obtain the conditional *Usp13* gain-of-function mice, the HFHC or WTDF diet-fed Rosa^{Usp13} mice were injected with a 1.5×10^{12} genome copies (gc) dose of an AAV8-TBG-Cre vectors *via* the tail vein to induce hepatocytes-specific *Usp13* overexpression (Hep^{Usp13}OE HFHC, Hep^{Usp13}OE WTDF). Rosa^{Usp13} mice given an equal dose of AAV empty vector were treated as controls (HepRosa HFHC, HepRosa WTDF).

2.5.4. Animal study design 4th

To further investigate the function of USP13 in NASH progression, full-length of mouse *Usp13* sequences or mouse *Usp13* sequences with UBA domain deletion were loaded in AAV8 vector to create AAV-TBG-*Usp13* or AAV-TBG-*Usp13* (ΔUBA) vectors. The Hep^{Usp13}KO mice were then injected with a 1.5×10^{12} genome copies (gc) dose of corresponding vectors to produce *Usp13* gain-of-function mice. These mice were further fed with a 24-week HFHC diet to induce NASH phenotype (Hep^{Usp13}GOF HFHC, Hep$^{Usp13(\Delta UBA)}$GOF HFHC). The corresponding mice were injected with blank vectors were used as controls.

2.5.5. Animal study design 5th

The male Hep$^{Usp13\text{-}Irhom2}$KO mice, Hep^{Usp13}KO mice, Hep^{Irhom2}KO mice and Flox mice were also treated with 24-weeks HFHC diet to produce NASH phenotype and estimate the physiopathological changes. Also, the corresponding littermates treated with NCD fodder for a same time period were regarded as control mice.

2.5.6. Animal study design 6th

To estimate the protection function of USP13 against NASH progression more deeply, Hep^{Irhom2}KO mice and Irhom2-floxed mice were injected with or without LV-sh*Usp13 via* liver portal vein to produce hepatocyte-specific *Usp13-Irhom2* dual functional loss mice or hepatocyte-specific *Usp13* functional loss mice before 24-weeks NASH diet administration (Hep^{Irhom2}KO HFHC) or halfway by NASH diet feeding (Hep^{Irhom2}KO/LV-sh*Usp13* HFHC, Flox/LV-sh*Usp13* HFHC).

2.5.7. Animal study design 7th

To obtain different NASH diet-induced steatohepatitis, Rosa^{Usp13} mice were treated a HFMCD diet for 8 weeks to create NASH phenotype. The Rosa^{Usp13} mice were injected with 1.5×10^{12} genome copies (gc) of AAV8-TBG-Cre vectors *via* the tail vein to induce hepatocytes-specific *Usp13* overexpression (Hep^{Usp13}OE HFMCD). Rosa^{Usp13} mice given an equal dose of AAV empty vector were treated as controls (HepRosa HFMCD).

2.6. Cell culture and administration

The L02 cell line were obtained and used in the current study as our previous reports described[13,24]. Cells associating with corresponding *in vitro* or *in vivo* experiments were compulsorily examined for mycoplasma interference *via* polymerase chain reaction detection. The L02 cells were cultured in DMEM medium (Cat.: BC-M-005, Bio-Channel Biotechnology Co., Ltd., China) containing 1% penicillin + streptomycin (Cat.: BL505A; Biosharp Life Sciences), 10% premium quality FBS (Cat.: 085-150, WISENT), and were maintained in a 5% CO_2, 37 °C directly-heated type cell incubator (SANYO). Mouse primary cultured hepatocytes used in this experiment were isolated and concentrated from indicated experiments' animals by liver perfusion. In brief, after anesthesia with sodium pentobarbital, mice abdominal cavity was opened. Then, the liver samples were tardily perfused with 1 × liver perfusion working solution (Cat.: 17701038, Gibco™) and 1 × liver digest working solution (Cat.: 17703034, Gibco™) *via* the portal vein. Then, the digested liver tissue was filtered using a 100 μm steel mesh. The primary isolated hepatocytes were produced by harvesting the filter solution after 800 rpm centrifugalization (Allegra V-15R, Beckman Coulter Life Sciences, Germany) (4 °C, 5−10 min), and next purified using percoll-solution (Cat.: 40501ES60, YEASEN, Shanghai, China).

The isolated hepatocytes were maintained in corresponding DMEM medium (10% FBS and 1% penicillin−streptomycin) and then cultured in a 37 °C, 5% CO_2 condition. To mimic hepatic lipid deposition and steatosis of *in vivo* experiments, the L02 cells and mouse primary isolated hepatocytes were administrated with the indicated dose of PA, TNF-α, IL-6, fructose, or OA to investigate the Usp13 protein expression or lipid accumulation of Ad*Usp13* or Adsh*Usp13*-transfected cells. The corresponding antibodies, reagents and chemicals used in this work are shown in Supporting Information Table S2.

2.7. Construction of the knockout cell lines

The establishment method of targeted gene-deletion cell lines participated in the work were constructed as described previously[13,24]. Briefly, cell lines with *Usp13 or Ubc13* ablation were established by CRISPR-Cas9 system. The designed small guide RNA (sgRNA) for human *USP13 or UBC13* gene were established and cloned into lentiCRISPR v2 vectors (Addgene, Watertown, MA, USA) to create the Cas9/sgRNA-loaded lentivirus. The oligo sequence fragment used for construction of sgRNA vector are indicated as: designed sg*USP13*-1: 5′-GACCTGGGCACGCGGATCGT-3′; designed sg*USP13*-2: 5′-GCATGGAGGCGGCAACCAACA-3′, designed sg*UBC13*-1: 5′-GGCGTTGCTCTCATCTGGTT-3′; designed sg*UBC13*-2: 5′-CCCTCAAAGGGGGAATCCTG-3′. Next, the packaging vectors pMD2.G and psPAX2, together with corresponding prepared small guide RNA (sgRNA) plasmids were then transfected into human embryonic kidney (HEK) 293T cells using Lipofectamine™ CRISPRMAX™ Cas9 (Invitrogen™) or FuGENE 6 Transfection Reagent (Promega Biotech Co., Ltd., China) for 45 h. Then, the L02 cells were treated with the prepared supernate-containing lentivirus to establish the targeting gene deletion cells. The cell clones-containing gene deficiency were distinguished by Western blotting.

2.8. Vectors preparation and transfection

To overexpress *USP13*, *Homo sapiens* full-length *USP13* cDNA expression vectors were constructed by PCR-based cDNA amplification, and then packed into the pcDNA3.1 3 × HA-tagged plasmids and the pcDNA3.1 3 × Flag-tagged plasmid (Addgene, Watertown, MA, USA), respectively. Abridged USP13 and IRHOM2 tiny fragments expression plasmids including IRHOM2-HA, USP13-Flag, USP13 (ΔUBP)-Flag, USP13 (ΔUBP/Cys-box)-Flag, USP13 (ΔUBP/UBA)-Flag, USP13 (ΔUBA/Cys-box)-Flag, USP13 (ΔUBA)-Flag, and IRHOM2 (ΔIRHD/TM)-HA, IRHOM2 (ΔTM)-HA, IRHOM2 (ΔIRHD)-HA, IRHOM2 (ΔN-Tail)-HA and IRHOM2 (ΔN-Tail/IRHD)-HA were accordingly prepared (Fig. 6B), and UBC13-Myc were constructed by general PCR approach, and were then loaded into indicated plasmids. The WT ubiquitin with Myc-tag expression plasmids were prepared ground on pcDNA3.1 plasmid. Next, ubiquitin and corresponding ramifications including ubiquitin in which the only intact amino acid (AA) residue was K48O-ubiquitin, K11O-ubiquitin, K63O-ubiquitin, K29O-ubiquitin, K33O-ubiquitin, K6O-ubiquitin and K27O-ubiquitin were then inserted into the pcDNA3.1 Myc-tag vector (Addgene, Watertown, MA, USA). Vectors were transfected into L02 cells *via* ViaFect™ Transfection Reagent (Cat.: E4982, Promega, Beijing, China) according to the product specification. Moreover, to further study the biological effects of USP13 *in vitro*, we have constructed corresponding adenovirus (Ad)-packaged targeted gene expression plasmids. *Homo sapiens* or *Mus musculus* full-length *USP13* sequences and designed short hairpin RNA (shRNA) targeting human or mouse *USP13* (sh*USP13*) (shRNA sequences RNA-1: GTGATTGAGATGGAGAATA; RNA-2: GGGAACATGTTGAAAGACA for human; RNA-1: TTGATATGGCAAACATAATGG; RNA-2: AACTGAGGTAGCAACTGTTGC), human WT *USP13* sequences with M664E/m739E mutation, and targeting human or mouse MISSION shRNA Plasmid DNA IRHOM2 (sh*IRHOM2*) obtained from Sigma−Aldrich (Cat.: SHCLND-NM-024599; Cat.: SHCLND-NM-172572) were respectively packaged into adenovirus (Ad*USP13*, Adsh*USP13*; Ad*IRHOM2*, Adsh*IRHOM2*) by Adeno-X™ Adenoviral System 3 Kit (Cat.: 632269, Takara Bio Inc.). The empty adenovirus (AdshRNA or AdGFP) was regarded as controls for expression suppression (knockdown) or overexpression, respectively. The achieved adenovirus (Ad) vectors were purified and titrated to 5×10^{10} PFU by Vivapure AdenoPACK (Cat.: VS-AVPQ022, Sartorius, Shanghai, China) according to the product specification. To generate the LV-*Usp13* or LV-sh*Usp13* vectors, the mouse *Usp13* cDNA sequences or shRNA targeting mouse *Usp13* sequences were loaded into pLenti-GFP-Puro-CMV or pLenti-U6-GFP (Addgene) to upregulate or downregulate USP13 expression *in vivo* experiments.

2.9. Metabolic factors and serum cytokines parameters

Triglyceride (TG) contents were quantified using Triglyceride (TG) Content Detection Kit (Cat.: D799795-0050, Sangon Biotech, Co., Ltd., Shanghai, China) or Triglyceride (TG) Assay Quantification Kit (Cat.: KA0847, Novus Biologicals) based on the product specification. The contents of blood glucose after experimental period were examined using universal glucose test strips (glucose oxidase method) (Lot.: 3558469, ONETOUCH Ultra, LifeScan, Inc., CA, USA). HOmeostasis Model Assessment for Insulin Resistance (HOMA-IR) index was quantified from fasting insulin and fasting blood glucose, respectively. The HOMA-IR index was exhibited and calculated as Eq. (1):

$$[\text{HOMA-IR} = \text{Fasting insulin} \times \text{Fasting blood glucose}/22.5] \quad (1)$$

The GTT detection protocols were performed according to our former reports[13,24]. Evaluation of mouse chemokines and cytokines were performed using corresponding commercially-available ELISA kits. The TNF-α (Cat.: ab100747), IL-1β (Cat.: ab197742), IL-10 (Cat.: ab255729), IL-6 (Cat.: ab222503), MCP-1 (Cat.: ab208979), IL-18 (Cat.: ab216165) and insulin (Cat.: ab285341) ELISA kits were purchased from Abcam. The contents of serum or tissue glutamic pyruvic transaminase (GPT/ALT) (Cat.: C009-2-1), glutamic oxalacetic transaminase (GOT/AST) (Cat.: C010-1-1), alkaline phosphatase (ALP/AKP) (Cat.: A059-1-1), total cholesterol (TC) (Cat.: A111-1-1), hepatic triglyceride (TG) (Cat.: A110-1-1), direct bilirubin (DBil) (Cat.: C019-2-1), total bilirubin (TBil) (Cat.: C019-1-1), γ-glutamyl transferase (GGT) (Cat.: C017-1-1) and non-esterified fatty acids (NEFA) (Cat.: A042-2-1) were quantified by commercially-available kits (Nanjing Jiancheng Bioengineering Institute, China) in the indicated experiment' groups based on the manufacturer's instructions.

2.10. Histopathological analysis

To perform histopathologic and immunohistochemical assay, the tissue was consequently fixed with 4% formaldehyde-tissue

fixative solution (Cat.: 80096618, Sinopharm Chemical Reagent Co., Ltd., China), embedded in paraffin wax (Cat.: 69018961, Sinopharm Chemical Reagent Co., Ltd., China), and then sectioned transversely. The tissue slices were subjected to H&E staining (Cat.: G1120, Hematoxylin−Eosin/HE Staining Kit, Solarbio Life Sciences, Beijing, China) to visualize the degree of lipid accumulation and hepatic inflammation. To further analyze hepatic lipid deposition, the slices were frozen in tissue opti-mum cutting temperature (O.C.T)-freeze medium (Cat.: C1400, Applygen Technologies, Inc., China) and then subjected to oil red O Kit (Cat.: PH1226, Scientific Phygene, China) for 10−15 min. After being washing with 60% isopropanol (Cat.: 40064360, Sinopharm Chemical Reagent Co., Ltd., China), the tissue slices were restained with haematoxylin. Moreover, to visualize collagen contents in liver tissue, slices were subjected to Masson's staining (Cat.: abs9348, Masson's Trichrome Stain Kit, Absin, Shanghai, China) and Sirius red staining (Cat.: PH1099, Enhanced Sirius Red Staining Kit, Scientific Phygene, China).

To perform immunohistochemical analysis, paraffin-embedded slices were dewaxed prior to incubation with primary antibodies including anti-IRHOM2 (Cat.: orb386934, Biobyt, dilution ratio 1/150−1/250), anti-USP13 (Abcam, Cat.: ab109264, dilution ratio 1/150−1/200), anti-F4/80 (Abcam, Cat.: ab16911, dilution ratio 1/150−1/200) or anti-CD11b (Abcam, Cat.: ab133357, dilution ratio 1/150−1/200) at 4 °C refrigeration overnight. The corresponding anti-rabbit IgG or anti-mouse IgG antibodies were used as the secondary antibody. All histological experiments were performed according to standard protocols presented in the reagent instructions and operation manual, and were performed by three histologists blinded to treatment procedures. Pictures were displayed using a light microscope (Leica, Germany) for samples section detection and a fluorescence microscope system (Leica, Germany) for immunofluorescence section detection.

2.11. *Glutathione S-transferase (GST) pull-down detection*

Direct protein binding between USP13 and IRHOM2 was carried out *via* the GST pull-down analyses according to our previous reports methods[13,24]. pGEx-4T-1/GST-*USP13* or pGEx-4T-1/GST-*IRHOM2* were constructed and transformed *via Rosetta* (DE3) competent cell system, then followed by activated with isopropyl *β*-D-thiogalactoside (IPTG) (Cat.: HY-15921, MedChemExpress, Shanghai, China).

2.12. *In vivo and in vitro binding ubiquitination detection*

The *in vivo* and *in vitro* binding ubiquitination detection were respectively operated in the current experiments according to the previous our protocols and methods[13,24]. Ubiquitination were investigated with a VIVAlink™ Ubiquitin Kit (Cat.: VB2952-50, Viva Bioscience, Exeter, UK) following procedures and protocols of the product manual.

2.13. *RNA extraction, quality control and high-throughput quantitative PCR (HT-qPCR)*

The whole RNA from indicated liver tissue or cells were separated by TRIeasy™ LS Total RNA Extraction (Cat.: 19201ES60, YEASEN, Shanghai, China) according to protocols recommended by product specification. The obtained RNA samples were stored at −80 °C for a maximum of 14 days. The absorption of RNA contents at 260 nm was confirmed using a Nanodrop photometer (Tecan) analysis. The best purity of RNA was guaranteed by determination of the 260 nm/280 nm adsorption ratio (values > 2.00). Accordingly, 1 μg of extracted RNA was inverse transcripted using Hifair II Reverse Transcriptase Kit (M-MLV) (Cat.: 11110ES93, YEASEN, Shanghai, China). The inverse transcription procedure was carried out at 42 °C for 1 h, followed by enzyme deactivation at 70 °C for 10 min. PCR process was carried out using Hieff qPCR SYBR Green Master Mix (YEASEN, Shanghai, China) in Agilent Mx3000P/Mx3005P Real-Time QPCR System (Agilent Technologies Inc.). The specific primer sequences for lipid metabolism, inflammation and fibrosis related key genes were generated by Sangon Biotech (Shanghai, China). The fold difference values were counted based on the $2^{(-\Delta\Delta Ct)}$ expression, where ΔCt indicates the difference in cycle thresholds between GAPDH and the target gene, and ΔΔCt indicates the relative alteration in the differences between indicated experimental groups and control groups.

To operate the high-throughput quantitative PCR (HTqPCR), the TaqMan Low Density Array (Cat.: P/N4342259, TLDA cards, Applied Biosystems, Germany) with 384-well micro fluidic cards were subjected to perform comparative analysis of gene expression in indicated groups, according to the operating manual & guides. The TLDA cards used in this study are customized by ABI Company according to the requirements of our experiment. The obtained cards were operated based on TaqMan chemistry where gene expression of a cluster of 384 genes were detected in 1 run. Also, the cards were prepacked with targeted TaqMan gene expression assays of importance for 127 inflammation-related genes, 57 lipid metabolism-related genes and 35 pro-fibrosis-related genes, and 6 controls were designed for normalization. The obtained gene expression alterations were standardized to the mean of 5 out of 6 controls (GAPDH, *β*-actin, *β*-tubulin, B2M, HPRT1) of the same dC_T sample, selected in accordance with their stability. Detected expression data from any one chosen group were regarded as an etalon (ddC_T) and data from all other groups were normalized to it. Gene expression levels were ultimately indicated as relative gene expression (presenting as 2^{-ddCT} fold change for result). TaqMan gene expression Master Mix (Cat.: P/N4369510, Applied Biosystems, Germany) was used when running the HT-qPCR. The ABI Prism SDS 2.1 software attached to ABI PRISM 7900HT systems was used to detect the data. The finally obtained results were presented as a heatmap image.

2.14. *Immunoblotting detection*

To perform immunoblotting analyses, liver tissue or cells were subjected to RIPA (radio immunoprecipitation assay) lysis buffer (Cat.: PH0317, Scientific Phygene) to yield lysates. Then, the final supernatant were compressed by centrifugation at 4 °C, 13,000 rpm for 30 min (H2500R-2, Cence, Hunan Xiang Yi Laboratory Instrument Development Co., Ltd., Changsha, China). Protein concentration of obtained supernatant was confirmed by BCA (bicinchoninic acid) Protein Quantification Kit (Cat.: 20201ES90, YEASEN, Shanghai, China) with fat-free BSA as a control. The total extracted protein samples were then processed to immunoblotting assay. The same amounts of total protein isolated from the indicated cells or liver samples were processed to 10% or 12% SDS/PAGE gel (Cat.: 20328ES50, SDS/PAGE Gel Preparation Kit, YEASEN, Shanghai, China) and then subjected to a 0.45 μmol/L Immun-Blot polyvinylidene fluoride (PVDF) membrane (Cat.: 10600023, Amersham Hybond, GE Healthcare Life Science, Germany) *via* wetting transfer method, followed by

Western blotting using the assigned primary antibodies. Subsequently, the immunoblotting membranes were incubated with blocking buffer (5% nonfat-dried milk) (Cat.: LP0033B, Biosharp Life Science, Beijing, China) in 1 × TBS working buffer solution (Cat.: PH1402, Scientific Phygene) containing 0.1% Tween-20 (Cat.: 9005-64-5, Sinopharm Chemical Reagent Co., Ltd., China) (1 × TBST working buffer solution) for 1 h, and mingled with the assigned primary antibodies at 4 °C refrigeration overnight. Then, the PVDF membranes were washed in 1 × TBST working buffer solution for 3 times, followed by co-treated with horseradish peroxidase-tagged goat anti-rabbit IgG (H + L) or anti-mouse IgG (H + L) (Cat.: 33201ES60; Cat.: 33101ES60, YEASEN, Shanghai, China) for 1−2 h at 25−30 °C. Immunoblotting membranes were visualized by New-SUPER (Hypersensitivity Type) ECL Kit (Cat.: KGP1128, KeyGen BioTECH, China) and exposed to FUJI Medical X-ray film (Cat.: 4741023952, FUJIFILM, China). Corresponding protein levels were then calculated as gray-scale score (Version 1.8.0, Microsoft Windows, Image J, NIH, USA) and normalized to GAPDH and standardized as a fold change of controls.

2.15. *Statistical analysis*

The associated results showed in this work were processed independently at least 3 times. All raw data involving this work were independently analyzed by suitable statistic protocols, as assigned in the figure legends. Unless otherwise stated, quantitative scores of data are presented as mean ± standard error of mean (SEM). ANOVA was used for comparison approach, multiple-group comparison was performed using *Dunnett's* multiple comparison test, and two-group comparison was performed using 2 tailed Student's *t* test. GraphPad Prism Software (Version 9.3.1.471 for Microsoft Windows 64-bit; GraphPad Software, San Diego, USA), the R packages and IBM SPSS Statistics (Version 25.0, Microsoft Windows, IBM, USA) were performed for the final data presentation. $P < 0.05$ means statistically significant difference.

3. Results

3.1. *Hepatocyte USP13 expression is inversely correlated with NASH severity in mouse model and human subjects*

To study the involvement of USP13 in the context of NASH, we primarily investigated its levels in liver tissue collected from high-energy diet and inherited obese mice model (*ob/ob* mice) with NASH pathological phenotype. We found that USP13 protein level profile was markedly lower in liver samples of 24-weeks HFHC diet-challenged mice and *ob/ob* mice than those of NCD diet-challenged mice and lean groups, respectively (Fig. 1A and B). Also, hepatic USP13 expression was gradually restrained in the livers (Fig. 1C and D) after HFHC challenge in time frame. Moreover, we further evaluated its expression in livers of patients with NAFLD and NASH pathology. Unsurprisingly, the markedly downregulated USP13 expression was markedly observed in individuals with simple hepatosteatosis and NASH phenotype compared to non-steatosis donors' group. Notably, the lower USP13 expressive abundance were further observed in the samples from NASH donors' cohort than those from only with simple hepatosteatosis (Fig. 1E and Supporting Information Fig. S1A). Meanwhile, the *in vitro* detection using inducer, *e.g.*, PA-, OA-, fructose-, TNF-α- and IL-6-triggered L02 cells also showed remarkable decrease in USP13 levels, as compared to the corresponding human groups (Fig. S1B). Furthermore, in human groups by Pearson correlation analyses, hepatic *Usp13* mRNA levels were inversely correlated with the hepatic *Irhom2*, *Tnfa* and *Il6* mRNA expression profiles, serum laminin (LN), total cholesterol (TC), γ-glutamyl transpeptidase (GGT), collagen type IV (IVC), alkaline phosphatase (AKP), blood glucose and body mass index (BMI) (Fig. 1F−H and Supporting Information Fig. S2A−S2F). Generally, the additional multiple linear regression and Pearson multiple correlation detection further determined the inverse relevance of hepatic USP13 expressive abundance with severity of NAFLD & NASH cohorts (Fig. 1I and Fig. S2G−S2J). To further highlight the negative correlation of USP13 expression with IRHOM2 levels, possible protein interaction prediction, in theory, between USP13 and IRHOM2 by GeneMANIA and String, and their coexpression by immunofluorescent labeling detection was displayed (Supporting Information Fig. S3A and S3B). Also, previous report has suspected that IRHOM2 could be modified by ubiquitination *via* potential regulator[17]. Indeed, significant increase in ubiquitination of IRHOM2, and occurrence of protein binding of USP13 and IRHOM2 in corresponding vectors-transfected L02 cells were further confirmed by co-immunoprecipitation (Co-IP) detection (Fig. S3C−S3E). Given the obvious changes of USP13 expression in fatty liver samples, we accordingly constructed an additional *in vitro* experiment using adenovirus (Ad)- or shRNA-induced *USP13* overexpression (Ad*USP13*) or *USP13* knockdown (Adsh*USP13*) to examine the biological effects of USP13 in regulating the critical features of hepatosteatosis, inflammation and IRHOM2 pathway (Supporting Information Fig. S4A). The transfected L02 cells were co-treated with NASH serum (mixture of fresh medium and serum isolated from NASH patients) or non-steatosis serum (mixture of fresh medium and serum isolated from non-steatosis donors) for 10 h. Certainly, detected by high-throughput quantitative PCR (HTqPCR) analysis, 127 and 57 genes involved in inflammatory response and lipid metabolism, selected according to their reported functions, were significantly and aberrantly expressed in the corresponding transfected L02 cells (Fig. S4B−S4D). Moreover, the intracellular TG detection and Oil red O staining showed that lipid deposition in NASH Serum or PA-treated Ad*USP13*-transfected L02 cells was markedly suppressed compared to those in the controls, accompanied by decreased concentrations of TG. In contrast, USP13 inhibition potentiated lipid deposition in transfected L02 cells. In addition, the aberrant expression changes in fatty acid metabolism and pro-inflammation-related key genes were also highlighted and observed in PA-induced transfected cells (Supporting Information Fig. S5A−S5D). The cells with USP13 overexpression dramatically restrained the processes involved in hyperactivation of Irhom2−MAP3K7 signaling pathway, which was further determined by Western blotting detection (Fig. S5E and S5F). The above findings reveal that USP13 may play a protective role in NASH pathologies.

3.2. *Usp13-mediated ex vivo gene therapy facilitates alleviation of HFHC-triggered NASH progression*

The validity of the HFHC challenge-induced NASH progression was confirmed in rodent model (Supporting Information Fig. S6A−S6D). Next, similar to the *in vitro* results, protein, and mRNA expression levels of IRHOM2 and USP13 *in vivo* showed

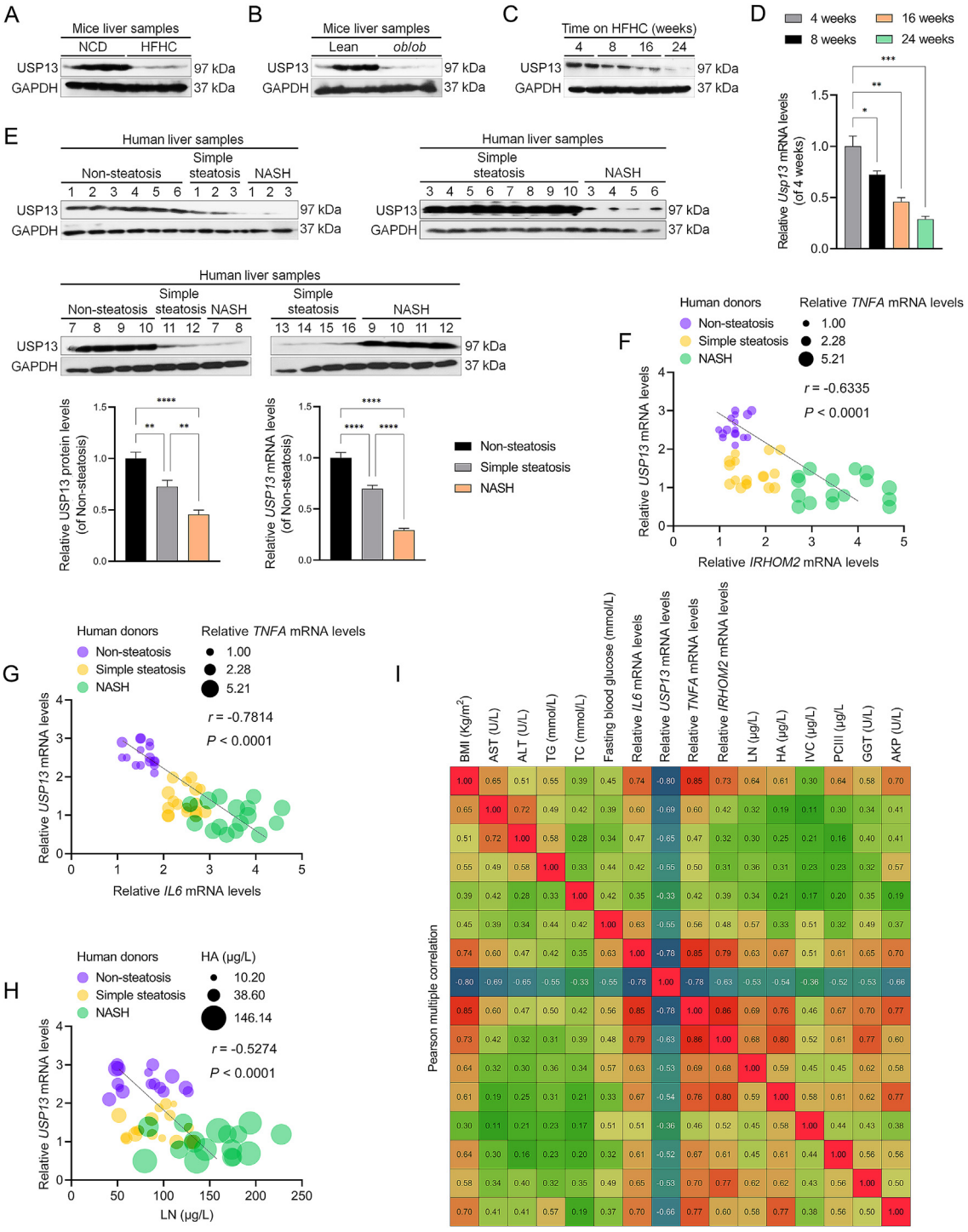

Figure 1 Hepatocytes USP13 activity is negatively correlated with NASH severity in human patients and rodent. (A, B) Representative immunoblotting bands of USP13 expression in the liver samples collected from male wildtype (WT) C57BL/6 mice that were fed with a NCD or HFHC diet for 24 weeks (A), or from *ob/ob* or lean mice (B) ($n = 4$ per group). (C, D) Representative immunoblotting bands of USP13 expression (C) and qPCR analysis of *USP13* mRNA levels (D) in the liver samples isolated from WT mice that were fed with a HFHC diet over time ($n = 4$ per group). (E) Representative immunoblotting bands and relative expression levels of USP13 in the liver samples of human donors with non-steatosis ($n = 16$ samples), simple steatosis ($n = 17$ samples) or NASH ($n = 16$ samples) phenotype. (F–H) Pearson correlation analyses indicating the correlations between human liver samples *USP13* mRNA expression and *IRHOM2* mRNA levels ($r = -0.6335$, $P < 0.0001$) (F), *IL6* mRNA levels ($r = -0.7814$, $P < 0.0001$) (G) and serum laminin (LN) ($r = -0.5274$, $P < 0.0001$) (H). mRNA expression is normalized to GAPDH levels. $P < 0.001$ for all of these correlations ($n = 49$ per indicator; $n = 147$ in total). (I) Pearson multiple correlation displaying the comprehensive correlation between human liver samples *USP13* mRNA expression and indicated parameter indexes ($n = 49$ per parameter). Data are expressed as mean ± SEM. The relevant experiments presented in this part were performed independently at least three times. $^{*}P < 0.05$, $^{**}P < 0.01$, $^{***}P < 0.001$, $^{****}P < 0.0001$.

completely opposite expression trends. Notably, in HFHC-induced mice NASH model, liver USP13 protein expressive abundance was inversely correlated with the serum ALT, AST, liver *Tnfa* mRNA levels, and liver IRHOM2 protein levels (Fig. S6E−S6J). The additional Pearson multiple correlation and multiple linear regression detection further identified that hepatic USP13 expression was inversely correlated with NASH severity in mice (Supporting Information Figs. S6K and S7A). Also, the potential protein interaction of USP13 and IRHOM2 in mice were predicted and showed by GeneMANIA and STRING (Fig. S7B). Meanwhile, mice primary cultured hepatocytes were transfected with Ad*USP13* or Adsh*USP13*, and co-treated with non-steatosis serum or NASH serum (Fig. S7C). Unsurprisingly, hepatocytes with USP13 overexpression, indeed, markedly suppressed lipid accumulation, intracellular TG levels and pro-inflammation-related genes expression, whereas USP13 inhibition significantly promoted these biological progresses, which was further confirmed by Oil red O staining and HTqPCR analyses (Fig. S7D−S7F). To better explore the protective function of USP13 in NASH *in vivo*, the *ex vivo* strategy of genetic therapy by lentivirus-packaged full-length *Usp13* cDNA sequence (LV-*Usp13*) or shRNA targeting *Usp13* (LV-sh*Usp13*) was employed to further study the role of USP13 on improvement of steatohepatitis (Fig. 2A). As expected, in *ex vivo* transplanted model, the HFHC-fed mice with hepatocyte-specific *Usp13* overexpression (HFHC LV-*Usp13*) did lead to prominent reduction in liver weight (LW), liver weight/body weight ratio (LW/BW), fasting blood glucose and corresponding HOMA-IR index, as compared to corresponding controls (HFHC LV-Control) (Fig. 2B and C). Also, the HFHC LV-*Usp13* mice had lower glucose levels than that in control groups, as determined by GTT data (Fig. 2D). We further indicated that the decreases of contents of liver TC, TG and NEFA were dramatically elevated in HFHC LV-*Usp13* mice (Fig. 2E). Furthermore, HFHC LV-*Usp13* mice showed more decreased steatosis in the livers than HFHC LV-Control mice (Fig. 2F−H). Consistently, liver CD11b and F4/80 positive inflammatory cells infiltration, HTqPCR analyses, hepatic function indicators, pro-inflammatory cytokines, Masson staining and Sirius red staining detection exhibited a significant reduction in liver inflammatory responses and collagen accumulation in HFHC LV-*Usp13* mice (Fig. 2I−M). However, in contrast to that, the HFHC-fed mice with LV-sh*Usp13* injection exhibited marked increase of liver weight (LW), liver weight/body weight ratio (LW/BW), fasting blood glucose, HOMA-IR index, blood glucose levels and liver lipid contents (Supporting Information Fig. S8A−S8G), as compared to those of HFHC LV-shRNA mice. Meanwhile, LV-sh*Usp13* mice with HFHC feeding also displayed more severe hepatosteatosis than control mice, as confirmed by the H&E staining, NAS score evaluation, Oil Red O staining (Fig. S8H−S8J). In addition, HFHC LV-sh*Usp13* mice also exhibited a remarkable upregulation in liver inflammation, aberrant genes expression involving fatty acid uptake and synthesis, *e.g.*, *Fatp1*, *Cd36, Fasn* and *Ppara*, and collagen deposition, as determined by hepatic CD11b and F4/80 positive inflammatory cells infiltration, qPCR analysis, liver function indicators, pro-inflammatory cytokines, Masson's staining and Sirius red staining (Fig. S8K−S8P) compared to the HFHC LV-shRNA control mice. These results indicate that NASH progression of the HFHC-induced mice is able to be significantly reversed by *Usp13*-mediated *ex vivo* gene therapy.

3.3. Hepatocyte-specific Usp13 loss facilitates HFHC/WTDF-mediated NASH

To explore the biological function of hepatocyte USP13 in NASH *in vivo*, here we constructed hepatocyte-specific *Usp13*-knockout mice (Hep^{Usp13}KO) (Supporting Information Fig. S9A) and subjected them to a HFHC or NCD feeding for consecutive 24 weeks. Immunoblotting analyses indicated that USP13 protein expression profile was dramatically suppressed in liver tissue of Hep^{Usp13}KO mice compared to those of Flox (*Usp13*-floxed) mice (Fig. S9B and S9C). After 24-weeks HFHC feeding administration, the Hep^{Usp13}KO mice displayed higher liver weight (LW) and liver weight/body weight ratio (LW/BW) than they were in HFHC-challenged Flox mice (Fig. 3A−C). Meanwhile, the Hep^{Usp13}KO mice exhibited higher fasting blood glucose (Fig. 3D), blood insulin levels and corresponding HOMA-IR index (Fig. 3E and F) than controls upon HFHC treatment. Impaired glucose tolerance in Hep^{Usp13}KO mice after HFHC ingestion was determined by glucose tolerance tests (GTTs) (Fig. 3G). Besides, the HFHC-fed Hep^{Usp13}KO mice further showed more severe hepatosteatosis than those in floxed control mice, as indicated by increased hepatic TG, TC and NEFA levels (Fig. 3H), Pearson correlation analysis (Fig. 3I and J), H&E staining (Fig. 3K and L), NAS score evaluation (Fig. 3M and N), Oil red O staining and HTqPCR analysis of lipid metabolism-related genes expression levels (Fig. 3O). Consistent with these, Hep^{Usp13}KO mice displayed a remarkable increase in hepatic inflammation, as evidenced by the liver CD11b^{+} and F4/80^{+} inflammatory cells infiltration and aberrant genes expression detected by HTqPCR analysis (Fig. 3P and Q). Liver collagen accumulation and the genes expression involved in fibrogenesis in the liver tissue were higher in HFHC-fed Hep^{Usp13}KO mice than that in the corresponding control mice, as indicated by Masson's staining, Sirius red staining and HTqPCR analysis (Fig. 3R). In addition, the serum concentrations of pro-inflammatory cytokines and hepatic function indices including TNF-α, IL-6, AST and ALT were dramatically higher in the HFHC Hep^{Usp13}KO mice than those of the HFHC-fed mice (Fig. 3S and T).

Given the pathogenesis of NASH identified as a heterogeneity disease, and NASH pathogenesis were triggered by the coaction of environmental and genetic factors, which could not be entirely reproduced in rodents[26]. Thus, we further investigated Usp13 function on the western-type diet plus 15% fructose (*w/v*)-drinking water (WTDF)-induced NASH model that mimics pathological phenotype of steatohepatitis. Consistent with the results obtained from the HFHC-fed mice, compared to the flox controls, indeed, the Hep^{Usp13}KO mice did not display significant alterations in body weight, but show higher liver weight (LW) and liver weight/body weight ratio (LW/BW) (Fig. S9D) after 24-weeks WTDF feeding. Furthermore, the fasting blood glucose, insulin levels, HOMA-IR index, hepatic lipid contents (TC, NEFA and TG), as well as the NAS score evaluation, inflammation, and collagen accumulation (Supporting Information Figs. S9E−S9L and S10A−S10D) were also markedly upregulated in the Hep^{Usp13}KO mice compared to control flox mice. Additionally, the severity of WTDF-mediated liver injury, as indicated by the aberrant gene expression involving lipid metabolism, inflammation and fibrogenesis-related crucial genes, and contents of serum pro-inflammatory cytokines and hepatic function indices, was significantly promoted in WTDF Hep^{Usp13}KO mice compared to

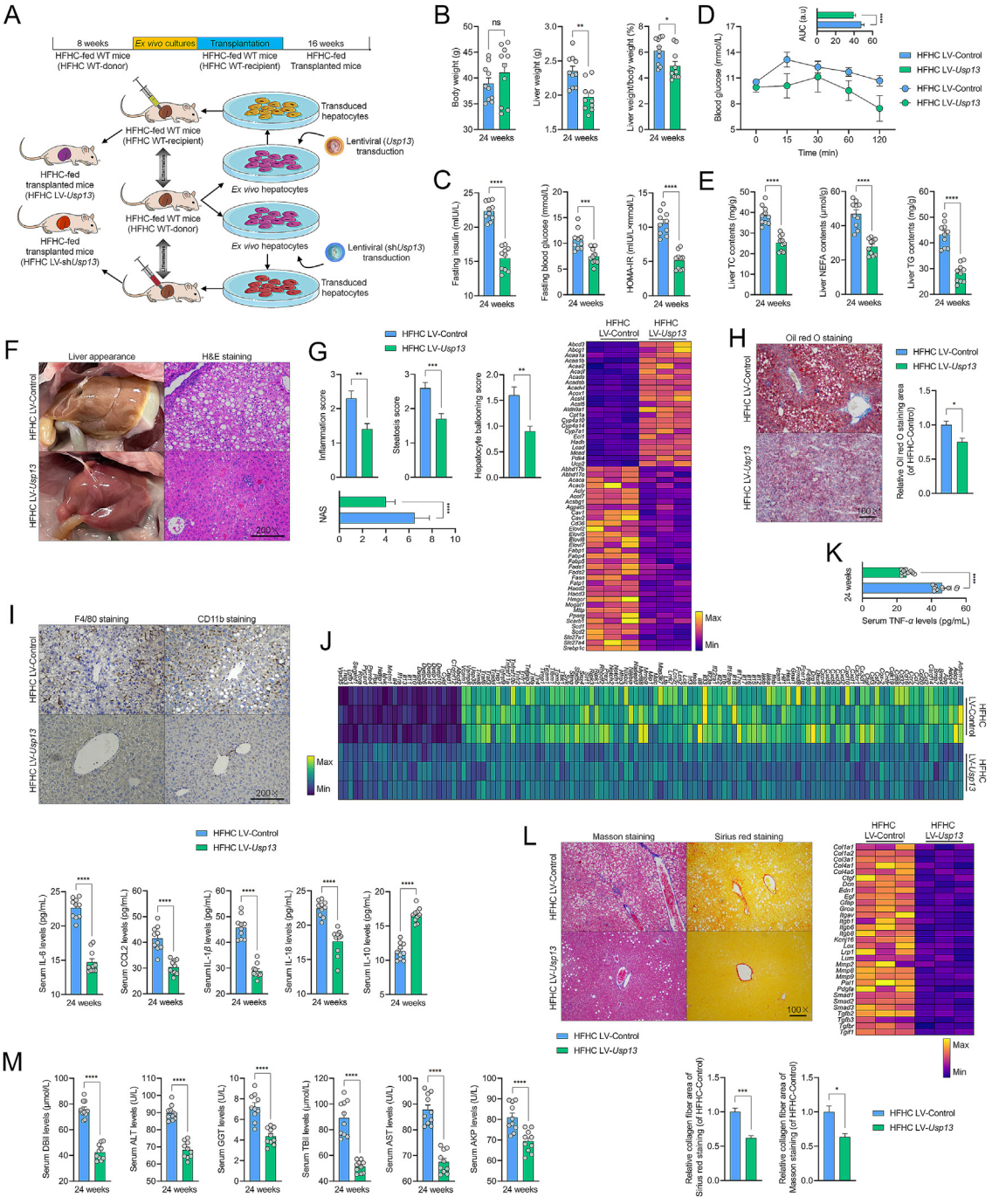

Figure 2 *Usp13* mediated-gene therapy mitigates NASH diet-induced lipid deposition, hepatic inflammation, and fibrosis. (A) Schematic diagram of experimental design for the *ex vivo*-mediated gene therapy. Primary hepatocytes from the preconditioned WT mice with an 8-weeks HFHC treatment as donor were isolated and *ex vivo* cultured. The cultured hepatocytes were transduced with lentivirus-loaded *Usp13* or sh*Usp13* sequences. The corresponding blank vectors were transduced as controls. Then, the additional HFHC-fed littermates mice as recipient were injected with transduced hepatocytes *via* portal vein. The HFHC-fed transplanted mice (HFHC LV-*Usp13* or HFHC LV-sh*Usp13*) were then fed with HFHC diet for additional 16 weeks. (B−D) Records for the body weight, liver weight and the ratio of liver weight/body weight (%) (B), fasting insulin levels, fasting blood glucose levels and HOMA-IR index (C) and glucose tolerance test (GTT) analysis (D) of the HFHC LV-*Usp13* mice at the last week of NASH diet treatment (n = 10 mice per group). (E) Liver lipid contents including TG, TC and NEFA of the HFHC LV-*Usp13* mice (n = 10 mice per group). (F, G) Representative pictures of liver appearance and H&E staining (F), and histological NAS score and HTqPCR analysis of lipid metabolism related genes expression changes (G) in the liver of HFHC LV-*Usp13* mice after *ex vivo* experiment (magnification, 200 ×; n = 10 images per group). (H, I) Representative pictures of Oil red O staining and immunohistochemical assay showing the lipid deposition (magnification, 100 ×) (H) and F4/80 or CD11b expression (magnification, 200 ×) (I) in liver of HFHC LV-*Usp13* mice after *ex vivo* experiment (n = 10 images per group for each staining). (J) HTqPCR analysis indicating the inflammation-related genes expression alteration in liver of HFHC LV-*Usp13* mice after *ex vivo* experiment (n = 10 per group). (K) Representative inflammation-related cytokines

corresponding controls (Fig. S10E−S10H). Finally, fat accumulation in viscera is always tightly associated with and connected with metabolic disorder. In fact, significant difference in food intake between the NCD- and HFHC/WTDF-fed Hep^{Usp13}KO mice was not significantly observed (Supporting Information Fig. S11A and S11B). However, the gain of visceral fat weight was enhanced in the HFHC/WTDF-fed Hep^{Usp13}KO mice, accompanied by a dramatically increase in the visceral fat weight/body weight ratio (Fig. S11C and S11D). Furthermore, fat cells size was extremely enlarged in HFHC/WTDF-fed Hep^{Usp13}KO mice, whereas significant difference between HFHC/WTDF-fed Hep^{Usp13}KO mice and HFHC/WTDF-fed flox controls was not detected (Fig. S11E and S11F). These findings further reveal that adipocyte proliferation might links to the increased weight of visceral fat in NASH diet-challenged mice.

3.4. *Hepatocyte-specific Usp13 overexpression mitigates HFHC/WTDF-triggered NASH*

Given the inverse relevance of USP13 expression with severity of NASH in mice model with USP13 loss-of-function experiments, based on Rosa26 conditional and/or inducible transgenesis, we accordingly established hepatocyte-specific *Usp13* overexpression *via Usp13* conditional knockin at the mouse locus of *Rosaβgeo26* (hereunder named as Rosa^{Usp13}) (Supporting Information Fig. S12A and S12B). The Rosa^{Usp13} mice subjected to AAV8-TBG-Cre injection were used to specifically overexpress USP13 in hepatocytes, followed by a 24-weeks administration with HFHC diet (Fig. 4A) (hereunder named as Hep^{Usp13}OE HFHC). The Rosa^{Usp13} mice with AAV8-TBG-Blank vector injection were served as controls (hereafter referred to as HepRosa HFHC). In contrast to the Hep^{Usp13}KO mice, the Hep^{Usp13}OE strain showed notably lower liver weight (LW) and LW/BW ratio than the Rosa^{Usp13} control mice after HFHC administration for continuous 24 weeks (Fig. 4B and C). No marked difference was recorded in body weight between Hep^{Usp13}OE and HepRosa groups during HFHC diet administration (Fig. 4B). Also, the abnormally elevated blood glucose, increased insulin levels and glucose intolerance were remarkably mitigated by Usp13 transgenic overexpression (Fig. 4D−G). More importantly, Hep^{Usp13}OE mice exhibited greatly decreased liver steatosis than they were in HepRosa mice after HFHC treatment, as determined by liver TG, TC and NEFA levels (Fig. 4H), Pearson analysis (Fig. 4I), liver appearance changes (Fig. 4J), H&E staining, NAS score (Fig. 4K and L), Oil red O staining and HTqPCR analysis of lipid metabolism-related genes expression levels (Fig. 4M and N). Compared to the HepRosa mice, Hep^{Usp13}OE mice also had repressive CD11b and F4/80 positive cell infiltration and pro-inflammatory genes than those in corresponding controls after HFHC treatment (Fig. 4O and P). Hepatic fibrosis and associated genes were downregulated in the HFHC-challenged Hep^{Usp13}OE mice compared with their HFHC-treated HepRosa control mice (Fig. 4Q and R). Meanwhile, pro-inflammatory cytokines and liver function indicators contents in serum (Fig. 4S and T) also were greatly reduced in Hep^{Usp13}OE mice during 24-weeks HFHC administration. We also subjected Hep^{Usp13}OE mice and corresponding HepRosa control mice to the WTDF diet for 24 weeks (Fig. S12C). WTDF diet-triggered increase of liver weight, lipid deposition, hepatic inflammation, collagen fibers accumulation and hepatic injury were markedly mitigated in Hep^{Usp13}OE mice (Supporting Information Figs. S12D−S12M and S13A−S3H). In addition, adipocytes size was concurrently dilated in HFHC- or WTDF-fed Hep^{Usp13}OE mice and HepRosa mice, but no marked changes in the indicated experimental groups (Supporting Information Fig. S14A−S14H). Collectively, our above findings confirm that USP13 is a strong blocker of NASH pathogenesis and its related metabolism dysregulation in mice.

3.5. *USP13 alleviates NASH pathogenesis by repressing IRHOM2−MAP3K7 signal cascade*

Considering the significant inhibitory effects of USP13 on NASH and its related pathogenesis phenotypes, the obtained results encouraged us to profoundly investigate the underlying molecular biological mechanism of USP13 and possible function. Increasing evidence has revealed that IRHOM2 signaling cascade was markedly activated in NAFLD/NASH progression. Among the examined crucial factors in IRHOM2-related signaling, marked activation of IRHOM2−MAP3K7 axis induced by NASH Serum or PA challenge was facilitated *in vitro*, but was remarkably restrained by USP13 overexpression (Fig. S5). Likewise, remarkably inverse correlation of USP13 expression with IRHOM2 abundance also has been confirmed (Fig. 1). Thus, to identify potential inhibitory function of USP13 on Irhom2 signaling, we accordingly generated hepatocyte-specific *Irhom2*-knockout (Hep^{Irhom2}KO) and hepatocyte-specific *Usp13* and *Irhom2* double deletion (Hep$^{Usp13\text{-}Irhom2}$DKO) mice (Supporting Information Fig. S15A−S15D), as indicated in Methods section. As expected, indeed, *Irhom2* deficiency blocked the USP13 deletion-mediated elevation of the IRHOM2−MAP3K7 signal and its downstream pathway cascades (Supporting Information Fig. S16A and S16B) in HFHC diet-induced NASH progression and greatly inhibited corresponding steatohepatitis. Of note, all of the NASH phenotypes that were promoted by *Usp13* deletion including liver weight gain, impaired glucose tolerance, dysregulated blood glucose levels, hepatic lipid deposition, elevated inflammation-related genes expression levels, collagen deposition, liver inflammation and hepatic injury were significantly mitigated by deficiency of Irhom2 expression (Fig. 5A−S). Moreover, the primary mouse hepatocytes transfected or co-transfected with/without Adsh*Usp13*, Adsh*Irhom2* or Adsh*Usp13*/Adsh*Irhom2* also exhibited lower intracellular TG levels during PA treatment (Fig. 5T).

To conclusively verify the biological role of USP13 on NASH development, we further constructed an additional *in vivo* NASH model. Similar to the *ex vivo* strategy, the Hep^{Irhom2}KO mice or

including TNF-α, IL-1β, IL-6, CCL2, IL-18 and IL-10 in serum from HFHC LV-*Usp13* mice and controls (n = 10 mice per group). (L) Representative pictures of Masson staining and Sirius red staining-indicated liver histopathologic changes, and HTqPCR analysis of fibrosis-related genes expression changes of the HFHC LV-*Usp13* mice after *ex vivo* experiment (magnification, 100 ×; n = 10 images per group for each staining). (M) Representative liver function-related indicators including direct bilirubin (DBil), total bilirubin (TBil), AST, ALT, AKP and GGT in serum from HFHC LV-*Usp13* mice and controls (n = 10 mice per group). Data are expressed as mean ± SEM. The relevant experiments presented in this part were performed independently at least three times. *P < 0.05, **P < 0.01, ***P < 0.001, ****P < 0.0001, ns., no significant difference.

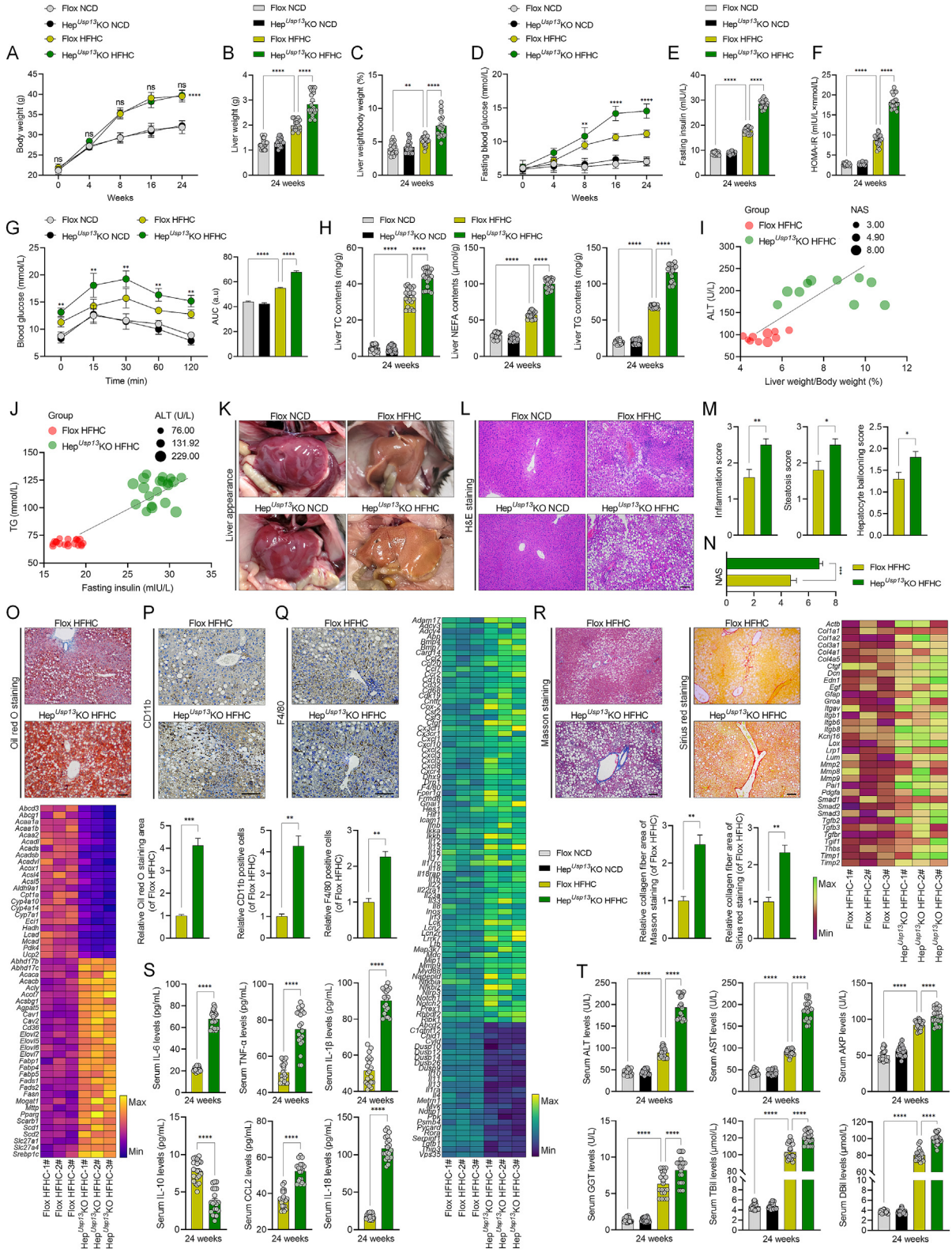

Figure 3 Hepatocyte-specific *Usp13* deletion aggravates HFHC/WTDF-induced NASH pathologies. (A–G) Records for the body weight (A), liver weight (B) and the ratio of liver weight/body weight (%) (C), fasting blood glucose levels (D), fasting insulin levels (E), HOMA-IR index (F) and glucose tolerance test (GTT) analysis (G) of the HFHC diet-fed Flox mice (Flox HFHC) or hepatocyte-specific *Usp13* deletion mice (Hep^{Usp13}KO HFHC), and NCD diet-fed corresponding controls ($n = 20$ mice per group). (H) Liver lipid contents including TG, TC and NEFA of the HFHC-fed Hep^{Usp13}KO or Flox mice ($n = 20$ mice per group). (I, J) Pearson correlation analyses indicating the correlations between ALT levels and ratio of liver weight/body weight (%) ($r = 0.6668$, $P < 0.0001$) (I), and TG levels and fasting insulin levels ($r = 0.926$, $P < 0.0001$) (J) in HFHC-fed Hep^{Usp13}KO or Flox mice. $P < 0.001$ for all of these correlations ($n = 10$ per parameter; $n = 30$ in total). (K–N) Representative

Irhom2$^{flox/flox}$ mice were subjected to LV-sh*Usp13* injection to establish hepatocyte-specific *Usp13-Irhom2* function loss mice or hepatocyte-specific *Usp13* function loss mice before 24-weeks NASH-provoking fodder administration, and or halfway by NASH diet feeding (Hep^{Irhom2}KO/LV-sh*Usp13* HFHC, Flox/LV-sh*Usp13* HFHC) (Fig. S15E). Unsurprisingly, after 24-weeks NASH-provoking diet treatment, remarkable hyperactivation of IRHOM2-MAP3K7 pathway, *e.g.*, phosphorylated MAP3K7, IκBα, JNK1/2 and NF-κB p65 was promoted in liver samples of *Irhom2*-floxed mice with LV-sh*Usp13* injection (Flox/LV-sh*Usp13*) but was significantly repressed in Hep^{Irhom2}KO and Hep^{Irhom2}KO/LV-sh*Usp13* groups (Fig. S16C and S16D). Besides, compared to HFHC-fed Flox/LV-sh*Usp13* mice, a series of phenotypes associated with NASH progression including abnormal gain of liver weight, dysregulated glucose tolerance, increased levels of blood glucose, hepatic lipid deposition, upregulated inflammation-, fibrogenesis-, and fatty acid synthesis-associated genes expression profile, serum pro-inflammatory factors, collagen deposition and hepatic injury were significantly alleviated in Hep^{Irhom2}KO and Hep^{Irhom2}KO/LV-sh*Usp13* mice (Supporting Information Figs. S15F−S15N and S17A−S17G). These results demonstrate that suppression of Irhom2−MAP3K7 signaling cascade mediated the repressive effects of USP13 on NASH development and physiopathological process.

3.6. *USP13 directly interacts with IRHOM2*

Given the blockage of IRHOM2-MAP3K7 axis by USP13 *in vivo* detection, we accordingly and widely studied the potential key factors that may be involved in USP13-mediated inhibition of IRHOM2−MAP3K7 signaling. Firstly, we indicated higher kinases activation in liver tissue of HFHC-treated Hep^{Usp13}KO mice, *e.g.*, MAP3K7, MEKK1, MEK1/2, MEK3 and MEK4, than those indicators in the HFHC-fed *Usp13*$^{flox/flox}$ mice (Supporting Information Fig. S18A), whereas these factors abundance were remarkably reduced by USP13 transgenic overexpression in HFHC-treated Hep^{Usp13}OE mice (Supporting Information Fig. S19A). Additionally, compared to that in their corresponding controls, the downstream pathways of MAP3K7 expression were markedly increased in Hep^{Usp13}KO mice (Fig. S18B), but those of these markers in Hep^{Usp13}OE mice were decreased after long-term HFHC challenge (Fig. S19B). Likewise, in line with our *in vivo* findings, the hyperactivation of IRHOM2−MAP3K7 axis and its related events of downstream cascades were elevated in isolated primary mouse hepatocytes transfected with Adsh*Usp13* (Fig. S19C and S19D), but significantly restrained in primary hepatocytes transfected with Ad*Usp13* after PA incubation (Fig. S19E and S19F). The decreased TG contents in PA-incubated Ad*Usp13*-transfected mouse primary cultured hepatocytes further determined our above results (Fig. S19G). Furthermore, in light of our *in vivo* study, the isolated primary mouse hepatocytes transfected with both of Adsh*Usp13* or/and Adsh*Irhom2* were accordingly subjected to NASH Serum or PA administration. As expected, Irhom2−MAP3K7 pathway and its downstream components, *i.e.*, phosphorylated MAP3K7 and JNK1/2/NF-κB in Adsh*Usp13*/Adsh*Irhom2* collectively transfected-mouse primary cultured hepatocytes exhibited lower pathway activation than they were in primary mouse hepatocytes only with Adsh*Usp13* transfection (Fig. S18C and S18D). In addition, consistent with *in vivo* results, the reduced TG contents, fatty acid synthesis- and uptake-, *e.g.*, *Acaca*, *Pparg*, *Fatp1* and *Fabp1*, and elevated fatty acid oxidation-, *e.g.*, *Pdk4* and *Ucp2*, associated genes expression profiles of transfected cultured hepatocytes were also dramatically observed (Fig. S18E−S18H).

In light of the function of USP13 on regulation of IRHOM2-related signaling pathway, the *in vivo* and *in vitro* data forced us to put forward another crucial concerns by which whether the USP13 binds with IRHOM2 in the context of NASH pathologies. Indeed, *in vitro* binding confirmed by immunoprecipitation (IP) detection suggested that ectogenous expression of USP13 has ability to directly interact with IRHOM2 and *vice versa* (Fig. S3E). To further explore this problem, the glutathione *S*-transferase pull-down assay was accordingly subjected to determine the interaction. As expected, a GST-conjugated IRHOM2 markedly pulled down USP13, and GST-conjugated USP13 also pulled down IRHOM2 (Fig. 6A). The results actually indicate that USP13 directly binds with IRHOM2. More importantly, USP13, a key member of deubiquitinating enzyme (DUB) families, is mainly composed of three domains: zinc finger UBP type (ZnF-UBP), cysteine-box (Cys-box) and two ubiquitin-associated domains (UBA1 and UBA2) (Fig. 6B). To identify which domain of USP13 is primarily in charge of the interaction with IRHOM2, a sequence of abridged mutants of *Homo sapiens* USP13 with Flag-tagged plasmids including wild-type USP13 (USP13-WT-Flag), ZnF-UBP domain deletion mutant (ΔUBP-Flag), ZnF-UBP and Cys-box domain double deletion mutant (ΔUBP/Cys-box-Flag), ZnF-UBP and UBA1/2 domain double deletion mutant (ΔUBP/UBA-Flag), UBA1/2 and Cys-box double ablation mutant (ΔUBA/Cys-box-Flag) and only UBA1/2 domain mutant (ΔUBA-Flag) plasmids were next created for the necessary interaction assay. The Co-IP detection in transfected L02 cells revealed that IRHOM2 was coprecipitated with USP13 (WT), USP13 (ΔUBP) and USP13 (ΔUBP/Cys-box). The present results demonstrate that the UBA domain in USP13 conduces its capacity to bind with IRHOM2. Accordingly, the following abridged mutants of IRHOM2 with HA-tagged plasmids including wild-type IRHOM2 (IRHOM2-

pictures of liver appearance (K) and H&E staining (L), and histological NAS score (M, N) changes in HFHC-fed Hep^{Usp13}KO or Flox mice (magnification, 100 ×; $n = 10$ images per group). (O) Representative pictures of Oil red O staining showing the lipid accumulation (upper) and HTqPCR analysis of lipid metabolism related genes expression changes (lower) in the liver of HFHC-fed Hep^{Usp13}KO or Flox mice (magnification, 100 ×; $n = 10$ images per group). (P, Q) Representative pictures of immunohistochemical assay showing the CD11b (P) or F4/80 (Q) expression (magnification, 200 ×) and inflammation-related genes expression changes in liver of HFHC-fed Hep^{Usp13}KO or Flox mice ($n = 10$ images per group for each staining). (R) Representative pictures of Masson staining and Sirius red staining-indicated liver histopathologic changes and fibrosis-related genes expression changes in liver of HFHC-fed Hep^{Usp13}KO or Flox mice (magnification, 100 ×; $n = 10$ images per group for each staining). (S) Representative inflammation-related cytokines including TNF-α, IL-1β, IL-6, CCL2, IL-18 and IL-10 in serum from HFHC-fed Hep^{Usp13}KO or Flox mice ($n = 20$ mice per group). (T) Representative hepatic function-related indicators including DBil, TBil, AST, ALT, AKP and GGT in serum from HFHC-fed Hep^{Usp13}KO or Flox mice ($n = 20$ mice per group). Data are expressed as mean ± SEM. The relevant experiments presented in this part were performed independently at least three times. *$P < 0.05$, **$P < 0.01$, ***$P < 0.001$, ****$P < 0.0001$, ns., no significant difference.

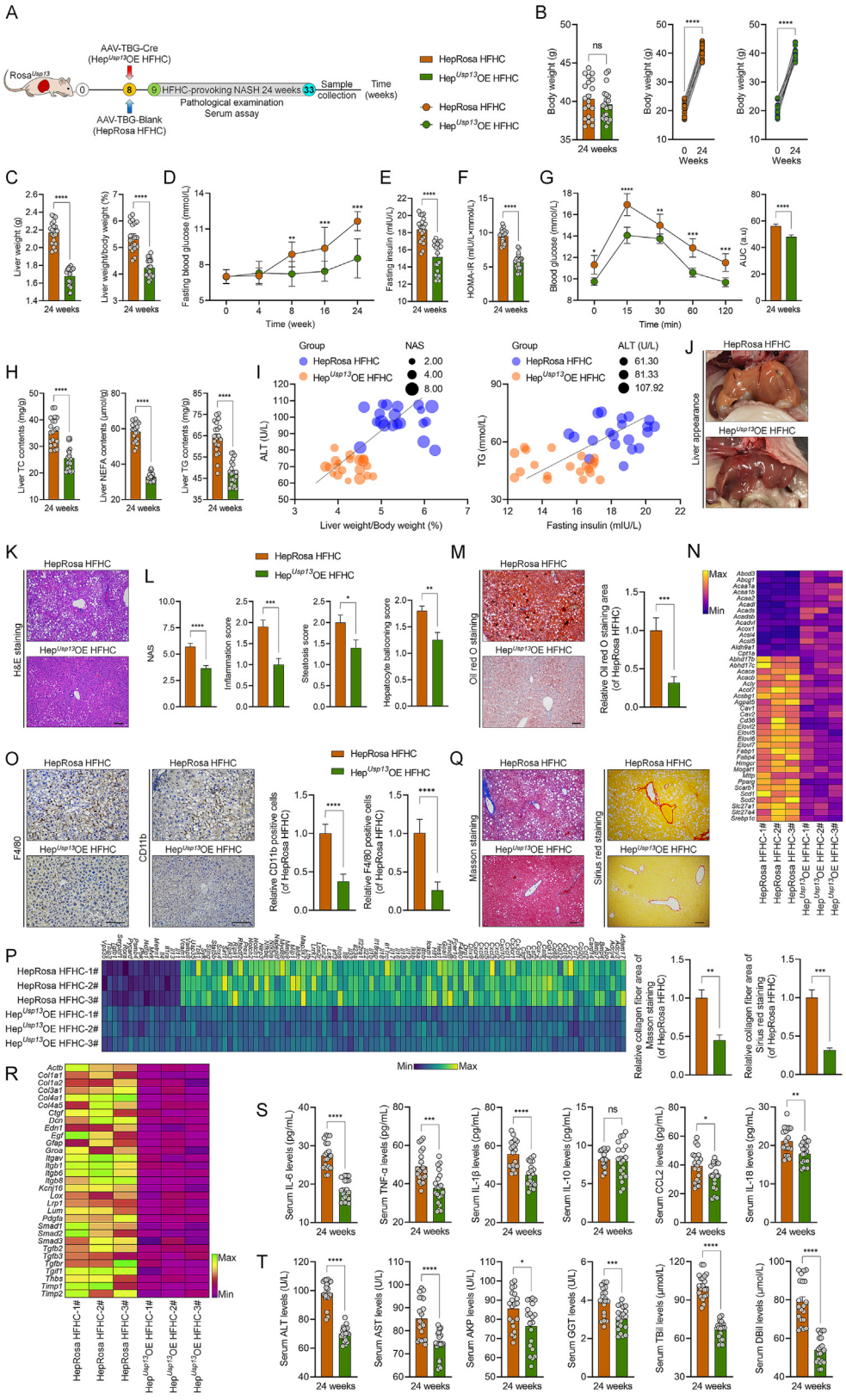

Figure 4 Hepatocyte-specific *Usp13* overexpression mitigates HFHC/WTDF-induced NASH pathologies. (A) Schematic diagram of adeno-associated virus (serotype 8)-TBG-Cre (AAV-TBG-Cre)-mediated *Usp13* overexpression in liver of HFHC-fed Rosa^{Usp13} mice (Hep^{Usp13}OE HFHC). The AAV-TBG-blank was used as control (HepRosa HFHC). (B−G) Records for the body weight (B), liver weight and the ratio of liver weight/body weight (%) (C), fasting blood glucose levels (D), fasting insulin levels (E), HOMA-IR index (F) and glucose tolerance test (GTT) analysis (G) of the Hep^{Usp13}OE HFHC and HepRosa HFHC mice (n = 20 mice per group). (H) Liver lipid contents including TG, TC and NEFA

WT-HA), IRHD and TM domain double deletion mutant (ΔIRHD/TM-HA), TM domain deletion mutant (ΔTM-HA), IRHD domain deletion mutant (ΔIRHD-HA), N-terminal tail domain deletion mutant (ΔN-Tail-HA) and N-terminal tail and IRHD domain double deletion (ΔN-Tail/IRHD-HA) vectors were also constructed. Co-IP examination with these corresponding IRHOM2 mutants indicated that IRHOM2 without domain of the N-tail loss its ability to interact with USP13. Thus, N-terminal cytoplasmic tail (Tail) domain of IRHOM2 was required for the protein interaction with USP13 (Fig. 6B). Notably, previous studies have indicated that USP13 with enzymatic inactive mutant in M664E of UBA1 domain and M739E of UBA2 domain did not perform its catalytic function in the ubiquitination of substrates[19−21,23]. Consistent with this, we generated Ad*USP13* with M664E/M739E mutant vector (Ad*USP13*(M664E/M739E)) to further investigate whether these mutations may impair protective function of USP13 against NASH phenotypes *in vitro*. As expected, compared with that in their controls, the lipid accumulation detected by intracellular TG contents and Oil red O staining was not decreased in the L02 cells transfected with Ad*USP13*(M664E/M739E), but significantly attenuated in Ad*USP13*-transfected L02 cells after PA treatment (Fig. S18I and S18J). Besides, the IRHOM2−MAP3K7 axis and its downstream key components in Ad*USP13*(M664E/M739E) transfected-L02 cells also did not show significant difference in suppression of signaling activation than those of AdGFP-transfected cells (Fig. S18K). Additionally, compared with the Ad*USP13*-transfected cells, the fatty acid synthesis-, uptake- (*e.g.*, *ACACA*, *PPARG*, *FATP1* and *FABP1*), and fatty acid oxidation- (*e.g.*, *PDK4* and *UCP2*) associated genes expression profiles in Ad*USP13*(M664E/M739E)-transfected L02 cells were not altered (Fig. S18L, S18M). The obtained results indicated that UBA domain of USP13 is essential for its suppressive effects in regulation of NASH development *via* IRHOM2 pathway.

3.7. *USP13−IRHOM2 interaction is necessary for USP13-triggered mitigation of NASH*

Given the close-knit correlation of IRHOM2 deactivation with ubiquitin-associated domains activity of USP13, to thoroughly study whether USP13−IRHOM2 interaction is necessary for the inhibitory function of USP13 against NASH progression, AAV8-TBG-loaded WT full-length *Usp13* sequences vectors (AAV-TBG-*Usp13*) and AAV8-TBG-loaded *Usp13* with UBA1/2 domain deletion vectors (AAV-TBG-*Usp13* (ΔUBA)) was generated and used again to further explore the influence of USP13 with UBA1/2 mutants on HFHC-induced NASH pathologies *in vivo* (Fig. S18N). The Hep^{Usp13}KO mice were injected with AAV-TBG-*Usp13* (Hep^{Usp13}GOF) or AAV-TBG-*Usp13* (ΔUBA) (Hep$^{Usp13(\Delta UBA)}$ GOF) to induce corresponding USP13 gain-of-function (GOF) expression, followed by 24-weeks NASH-provoking HFHC diet feeding. The Hep^{Usp13}KO mice injected with AAV-TBG-Blank vectors were served as controls (HepControl). Unsurprisingly, the mice with AAV-TBG-*Usp13* (ΔUBA) injection did not reduce HFHC diet-mediated lipid deposition and liver inflammation as compared to those in control mice (Fig. S18O, S18P). Meanwhile, in parallel, after 24-weeks HFHC administration, the gain of liver weight, inflammation-related indicators, increased liver lipid contents, collagen accumulation, and IRHOM2−MAP3K7 pathway in Hep$^{Usp13(\Delta UBA)}$ GOF groups were not consistent with the mice in Hep^{Usp13}GOF groups, and also not displayed a marked alteration compared with HepControl mice groups (Supporting Information Figs. S20A−S20F and S21A−S21E). These data reveal that the USP13 directly interacts with IRHOM2 and prohibits its downstream signaling cascade in a UBA domain-dependent manner.

3.8. *USP13 inhibits IRHOM2 by deactivating UBC13-mediated K63 ubiquitination*

Previous study has indicated that IRHOM2 is ubiquitinated, and upregulation of IRHOM2 ubiquitination induced by UBC13 *via* K63 linkage significantly promoted TACE maturation and TNF-α release[12,13]. Indeed, the markedly increased ubiquitination of IRHOM2 in livers of NASH patients were observed, as compared to those of non-steatosis donors (Fig. S3C). The USP13, an important member of the deubiquitinating enzyme (DUB) superfamily, has been determined an IRHOM2-related protein and potential suppressor of IRHOM2 in our current work (Fig. 6A and B). Thus, we speculated that whether USP13 inhibited IRHOM2 expression by removing UBC13-mediated IRHOM2 K63-linked ubiquitination. Indeed, we indicated that the IRHOM2 ubiquitination in liver tissue were upregulated during HFHC treatment, accompanied by reduced USP13 expression, but were further exacerbated by USP13 ablation (Fig. 6C). The increase of IRHOM2 ubiquitination promoted by PA treatment was also determined in the cultured mice primary hepatocytes (Fig. 6D). Meanwhile, previous reports have indicated IRHOM2 may be modified by ubiquitination of K63 linkage[12,13]. Consistent with the results, the IRHOM2 was ubiquitinated with K63-linkage in

of the HFHC-fed Hep^{Usp13}OE or control mice ($n = 20$ mice per group). (I) Pearson correlation analyses indicating the correlations between ALT levels and ratio of liver weight/body weight (%) ($r = 0.6927$, $P < 0.0001$) (left), and TG levels and fasting insulin levels ($r = 0.5368$, $P < 0.0001$) (right) in Hep^{Usp13}OE HFHC and HepRosa HFHC mice. $P < 0.001$ for all of these correlations ($n = 20$ per parameter; $n = 60$ in total). (J−L) Representative pictures of liver appearance (J) and H&E staining (K), and histological NAS score (L) changes in Hep^{Usp13}OE HFHC and HepRosa HFHC mice (magnification, 100 ×; $n = 10$ images per group). (M, N) Representative pictures of Oil red O staining displaying the lipid accumulation (M) and HTqPCR analysis of lipid metabolism related genes expression changes (N) in the liver of Hep^{Usp13}OE HFHC and HepRosa HFHC mice (magnification, 100 ×; $n = 10$ images per group). (O, P) Representative pictures of immunohistochemical assay showing the F4/80 or CD11b (O) expression (magnification, 200 ×) and inflammation-related genes expression changes (P) in liver of Hep^{Usp13}OE HFHC and HepRosa HFHC mice ($n = 10$ images per group for each staining). (Q, R) Representative pictures of Masson staining and Sirius red staining-indicated liver histopathologic changes (Q) and fibrosis-related genes expression changes (R) in liver of Hep^{Usp13}OE HFHC and HepRosa HFHC mice (magnification, 100 ×; $n = 10$ images per group for each staining). (S) Representative inflammation-related cytokines including TNF-α, IL-1β, IL-6, CCL2, IL-18 and IL-10 in serum from Hep^{Usp13}OE HFHC and HepRosa HFHC mice ($n = 20$ mice per group). (T) Representative hepatic function-related indicators including DBil, TBil, AST, ALT, AKP and GGT in serum from Hep^{Usp13}OE HFHC and HepRosa HFHC mice ($n = 20$ mice per group). Data are expressed as mean ± SEM. The relevant experiments presented in this part were performed independently at least three times. *$P < 0.05$, **$P < 0.01$, ***$P < 0.001$, ****$P < 0.0001$, ns., no significant difference.

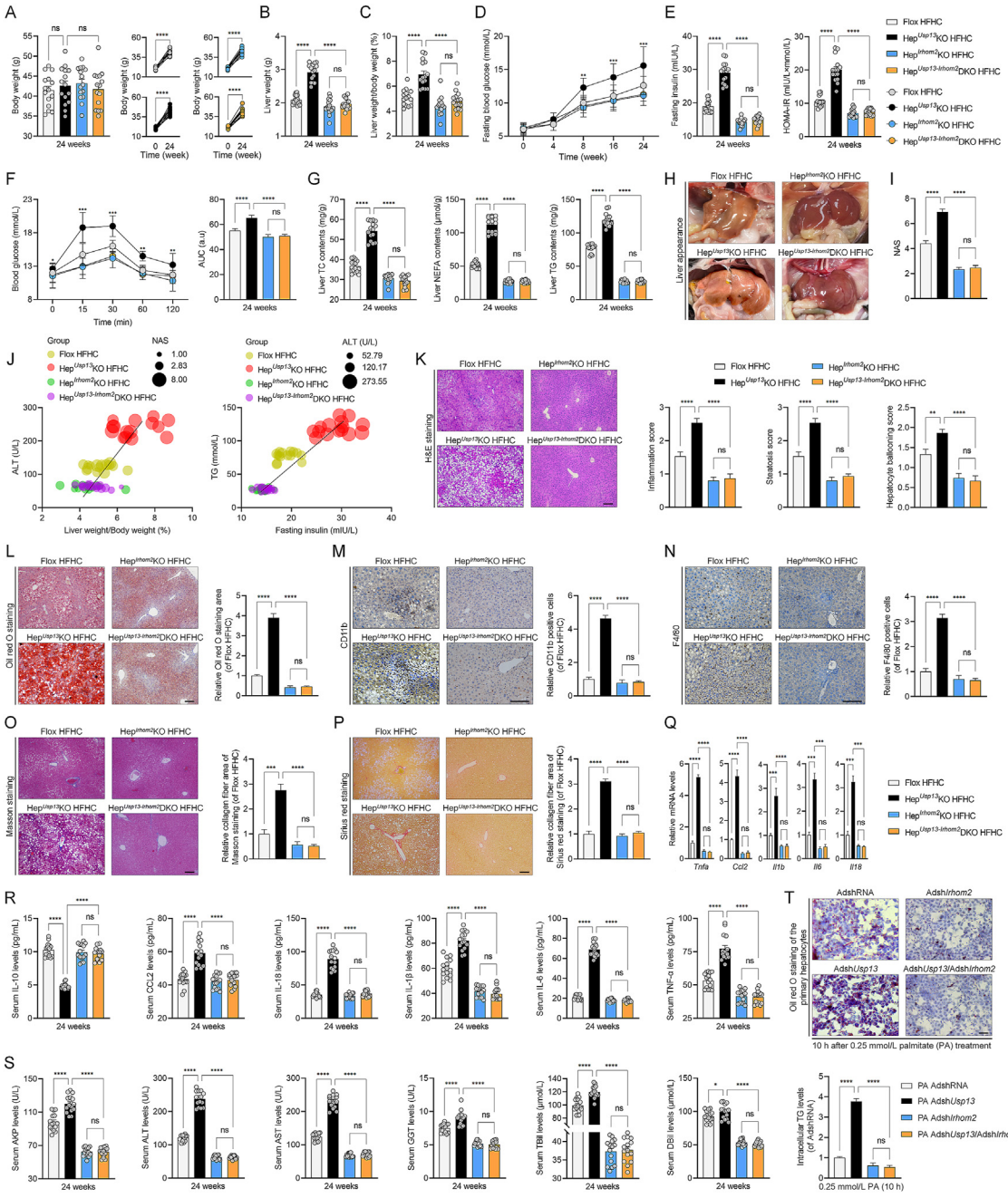

Figure 5 Irhom2 signaling is required for the protective function of USP13 against NASH diet-induced steatohepatitis. (A−F) Records for the body weight (A), liver weight (B) and the ratio of liver weight/body weight (%) (C), fasting blood glucose levels (D), fasting insulin levels, HOMA-IR index (E) and glucose tolerance test (GTT) analysis (F) of the HFHC-fed Hep^{Usp13}KO mice, hepatocyte-specific Irhom2 deletion (Hep^{Irhom2}KO) mice, hepatocyte-specific USP13 and Irhom2 double knockout (Hep$^{Usp13\text{-}Irhom2}$DKO) mice and Flox mice (n = 15 mice per group). (G) Liver lipid contents including TG, TC and NEFA of the Hep^{Usp13}KO HFHC, Hep^{Irhom2}KO HFHC, Hep$^{Usp13\text{-}Irhom2}$DKO HFHC and Flox HFHC group (n = 15 mice per group). (H, I) Representative pictures of liver appearance (H) and histological NAS score (I) changes in indicated HFHC-fed mice (n = 10 images per group). (J) Pearson correlation analyses showing the correlations between ALT levels and ratio of liver weight/body weight (%) (r = 0.7604, P < 0.0001) (left), and TG levels and fasting insulin levels (r = 0.9211, P < 0.0001) (right) in Hep^{Usp13}KO HFHC, Hep^{Irhom2}KO HFHC, Hep$^{Usp13\text{-}Irhom2}$DKO HFHC and Flox HFHC group. P < 0.001 for all of these correlations (n = 15 per parameter; n = 45 in total). (K−P) Representative pictures of H&E staining (K), Oil red O staining (L), immunohistochemical analysis of CD11b (M) and F4/80 (N) (magnification, 200 ×), Masson staining (O) and Sirius red (P) staining-indicated histological changes in liver of Hep^{Usp13}KO HFHC, Hep^{Irhom2}KO HFHC, Hep$^{Usp13\text{-}Irhom2}$DKO HFHC and Flox HFHC group (magnification, 100 ×; n = 10 images per group for each staining). (Q) qPCR analysis showing the pro-inflammation-related key genes including *Tnfa*, *Ccl2*, *Il1b*, *Il6* and *Il18* mRNA expression levels in indicated groups (n = 15 per group). (R) Representative inflammation-related cytokines including TNF-α, IL-1β, IL-6, CCL2, IL-18 and IL-10 in serum from indicated groups (n = 15 mice per group). (S) Representative hepatic function-related indicators including DBil, TBil, AST, ALT, AKP and GGT in serum from indicated groups (n = 15 mice per group). (T) Representative Oil red O staining images and intracellular TG levels

PA-treated L02 cells. More importantly, to exactly explore the process of USP13-regulated IRHOM2 ubiquitination, the plasmids with ubiquitin mutation K63, K48, K27, K11, K6, K33 and K29 were used for *in vitro* transfection detection. The tail-tag of "O" of mutation vectors indicated ubiquitin in which all Lys residues except themselves were absolutely mutated. Thus, we confirmed that in WT L02 cells, IRHOM2 was predominately by K63 ubiquitination upon PA administration, and this ubiquitination was dramatically reduced by USP13 intervention (Fig. 6E−H). On the contrary, Adsh*Usp13*-transfected primary mouse hepatocytes exhibited higher levels of K63-linked IRHOM2 ubiquitination during PA treatment than those of PA-incubated AdshRNA-transfected controls (Fig. 6I). Also, in line with *in vivo* data, mutation of USP13 (M664E/M739E) notably lost its ability to reduce Irhom2 ubiquitination in PA-induced *USP13*-deficient L02 cells (Fig. 6J). Based on the K63-linked Irhom2 ubiquitination mediated by Ubc13 as reported previously[16], we further investigated the expression alterations of UBC13 *in vivo* and *in vitro*. As expected, the livers of subjects with NASH or simple steatosis phenotype, and L02 cells induced by OA and PA treatment displayed higher UBC13 protein expression than their corresponding non-steatosis subject controls or BSA-treated L02 cells controls (Supporting Information Fig. S22A and S22B). Elevated UBC13 protein levels in WT mice and Hep^{Usp13}KO mice after 24-weeks HFHC or WTDF ingestion were also determined by western blotting detection (Fig. S22C and S22D). The UBC13 overexpression was able to markedly increase K63-linked ubiquitination of IRHOM2 in PA-induced UBC13-deficient L02 cells (Fig. S22E). Finally, the interaction of USP13, UBC13 and IRHOM2 was detected in the L02 cells. As indicated in Fig. 6K and L, the overexpression of USP13, but not USP13 (M664E/M739E), blocked the PA-triggered interaction of IRHOM2 and UBC13. Also, we further indicated that *UBC13*-deletion dramatically decreased IRHOM2 ubiquitination, and USP13 could not exhibit suppressive effect on IRHOM2 ubiquitination in these *in vitro* experiments (Fig. 6M).

3.9. *Hepatocyte-specific Usp13 overexpression alleviates HFMCD-induced NASH*

Based on the different molecular mechanisms and pathogenesis of NASH progression induced by HFMCD diet and another high-energy diet (*i.e.*, HFHC and WTDF), this forced us to further explore whether USP13 could also protect against HFMCD-induced NASH as well as HFHC/WTDF-induced model. Accordingly, the Rosa^{Usp13} mice injected with AAV-TBG-Cre vectors were used to overexpress USP13 abundance only in hepatocytes, followed by a HFMCD fodder feeding for 8 weeks (Fig. 7A) (hereafter referred to as Hep^{Usp13}OE HFMCD). The Rosa^{Usp13} mice with AAV8-TBG-Blank vector injection were served as controls (hereafter referred to as HepRosa HFMCD). Indeed, in addition to promptly activating lipid toxicity-triggered NASH pathogenesis, the HFMCD diet feeding leads to marked weight loss in mice model. However, weight loss in Hep^{Usp13}OE mice upon the HFMCD treatment was remarkably limited and later improved by USP13 overexpression (Fig. 7B). And equally surprising, Hep^{Usp13}OE mice also displayed notably reduced liver steatosis than they were in HepRosa mice after 8 weeks of HFMCD diet administration, as detected by liver TG levels (Fig. 7C), Pearson analysis, H&E staining, NAS score evaluation (Fig. 7D−F), Oil red O staining (Supporting Information Fig. S23A), HTqPCR analysis of lipid metabolism-related key genes expression and hepatic collagen contents (Fig. S23B−S23D). Besides, compared to the HFMCD-fed HepRosa mice, Hep^{Usp13}OE mice also had decreased liver fibrosis, suppressive F4/80 positive inflammatory cell infiltration, pro-inflammatory and fibrogenesis-associated key genes than those in corresponding controls in response to HFMCD treatment (Supporting Information Fig. S24A−S24F). Meanwhile, serum contents of liver function indicators and proinflammatory cytokines also were significantly downregulated in HFMCD diet-induced Hep^{Usp13}OE mice (Fig. S24G and S24H). In the same way, the IRHOM2−MAP3K7 signaling pathway, *e.g.*, phosphorylated MAP3K7, IκBα and NF-κB were further repressed in Hep^{Usp13}OE mice compared to that in controls (Fig. S24I). These results indicate that overexpression of USP13 is permissive for weight homeostasis, and USP13 is also critical for improvement of NASH progression induced by HFMCD diet feeding.

4. Discussion

Metabolism stress-associated liver disease commonly occurs in overnutrition ingestion-driven obesity and type II diabetes and identifies originally as NAFLD that can significantly facilitate this progress to NASH phenotype[1−3]. Indeed, the failure of the application of clinical drugs for NASH treatment and the slow process in development are mainly attributed to the poor understanding of the complicated pathogenesis of NASH[27]. Undoubtedly, a comprehensive and in-depth understanding of the molecular pathogenesis and progression of NASH, and the search for the potential promising target and effective drugs for this therapeutic target has become the highest priority for the treatment of NASH. In our current work, we identified USP13 of hepatocytes as a novel suppressor of NASH pathologies. *In vivo* study, to identify liver USP13 as a potent suppressor of overnutrition-triggered NASH pathologies, a series of mice model were constructed by using hepatocyte-specific *Usp13* knockout (Hep^{Usp13}KO), *Rosaβgeo26*-driven transgenic mice (Hep^{Usp13}OE) and lentivirus (LV)-induced *Usp13 ex vivo* genes therapy (LV-*Usp13*) mice to determine the protective effects of USP13 on HFHC-, WTDF- or HFMCD diet-induced steatohepatitis. We found that after a long-term HFHC/WTDF administration, dysfunctional USP13 in hepatocytes significantly promoted hepatic steatosis, liver inflammation, and hepatofibrosis. In contrast, hepatocytes with USP13 protein overexpression markedly restrained the NASH-related phenotype alterations in the liver. Mechanistically, liver USP13 could directly interact with IRHOM2 and dismantle its metabolic stress-triggered K63-linked ubiquitination by ubiquitin-conjugating enzyme UBC13. The USP13-induced deubiquitination repressed the downstream

showing the 10 h-lipid accumulation after 0.25 mmol/L PA-treated primary hepatocytes that were transfected or co-transfected with Adsh*Usp13*, Adsh*Irhom2* or Adsh*Usp13*/Adsh*Irhom2*. The hepatocytes transfected with AdshRNA (scrambled) was used as control (magnification, 100 ×; $n = 10$ images per group). Data are expressed as mean ± SEM. The relevant experiments presented in this part were performed independently at least three times. *$P < 0.05$, **$P < 0.01$, ***$P < 0.001$, ****$P < 0.0001$, ns., no significant difference.

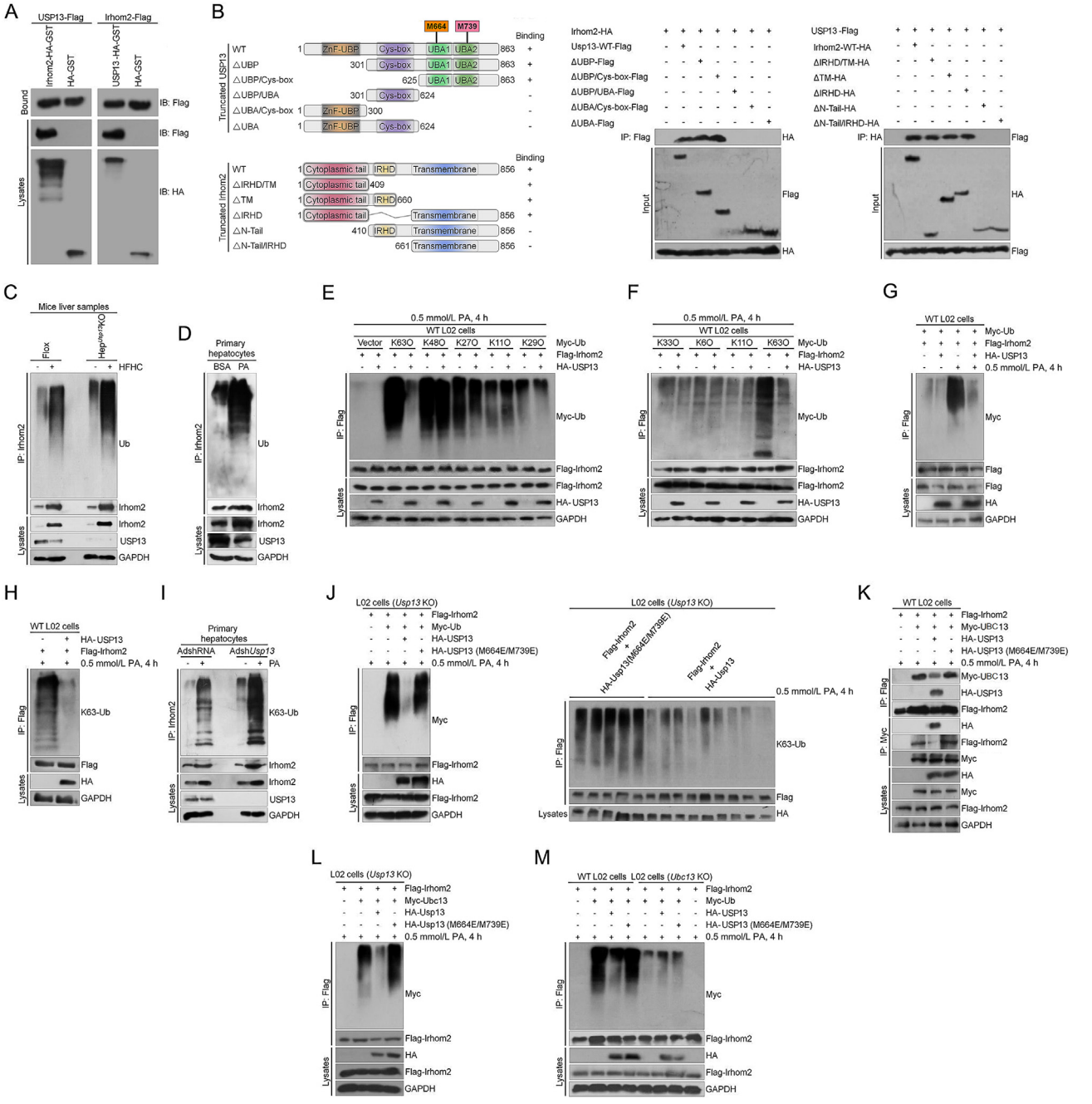

Figure 6 USP13 interacts with Irhom2, and USP13 removes Irhom2 K63-linked ubiquitination mediated by ubiquitin-conjugating enzyme Ubc13. (A) Representative immunoblotting bands for GST precipitation displaying USP13−Irhom2 binding by incubating purified USP13-flag with purified Irhom2-GST or by incubating Irhom2-flag with purified USP13-GST *in vitro*. Purified GST was regarded as a control. (B) Schematic of human full-length and truncated USP13 and Irhom2 (left), and representative immunoblotting mapping analyses indicating the interaction domains of USP13 and Irhom2 (right). (C) Representative immunoprecipitation analysis showing the ubiquitination levels of Irhom2 in the Flox mice and Hep^{Usp13}KO mice livers in the presence or absence of HFHC treatment of 24 weeks ($n = 4$ mice per group). (D) Ubiquitination levels of Irhom2 in 0.5 mmol/L PA-treated primary hepatocytes for 4 h. (E, F) Ubiquitination levels of Irhom2 after HA-USP13 overexpression and in response to 0.5 mM PA administration in WT L02 cells co-transfected with Flag-Irhom2 and the indicated Myc-tagged ubiquitin constructs (K48O, K63O, K33O, K6O, K29O, K27O, K11O). The tail label "O" means ubiquitin in which all lysines except itself were mutated. The empty vector was used as control. (G, H) Representative immunoprecipitation and Western blotting assays of the indicated proteins in the WT L02 cells transfected with HA-USP13, Flag-Irhom2 or Myc-Ub vectors in response to PA administration. (I) K63-linked ubiquitin (K63-Ub) and corresponding Irhom2 expression in primary hepatocytes transfected with AdshRNA or Adsh*Usp13* in the presence or absence of PA. (J) Representative immunoprecipitation and immunoblotting assays of the indicated proteins in the *Usp13*-deletion (*Usp13* KO) L02 cells transfected with HA-USP13, HA-USP13 (M664E/M739E), Flag-Irhom2 and Myc-Ub vectors in response to PA administration. (K) Representative immunoprecipitation and immunoblotting bands showing the possible interactions between Myc-Ubc13, HA-USP13, HA-USP13 (M664E/M739E) and

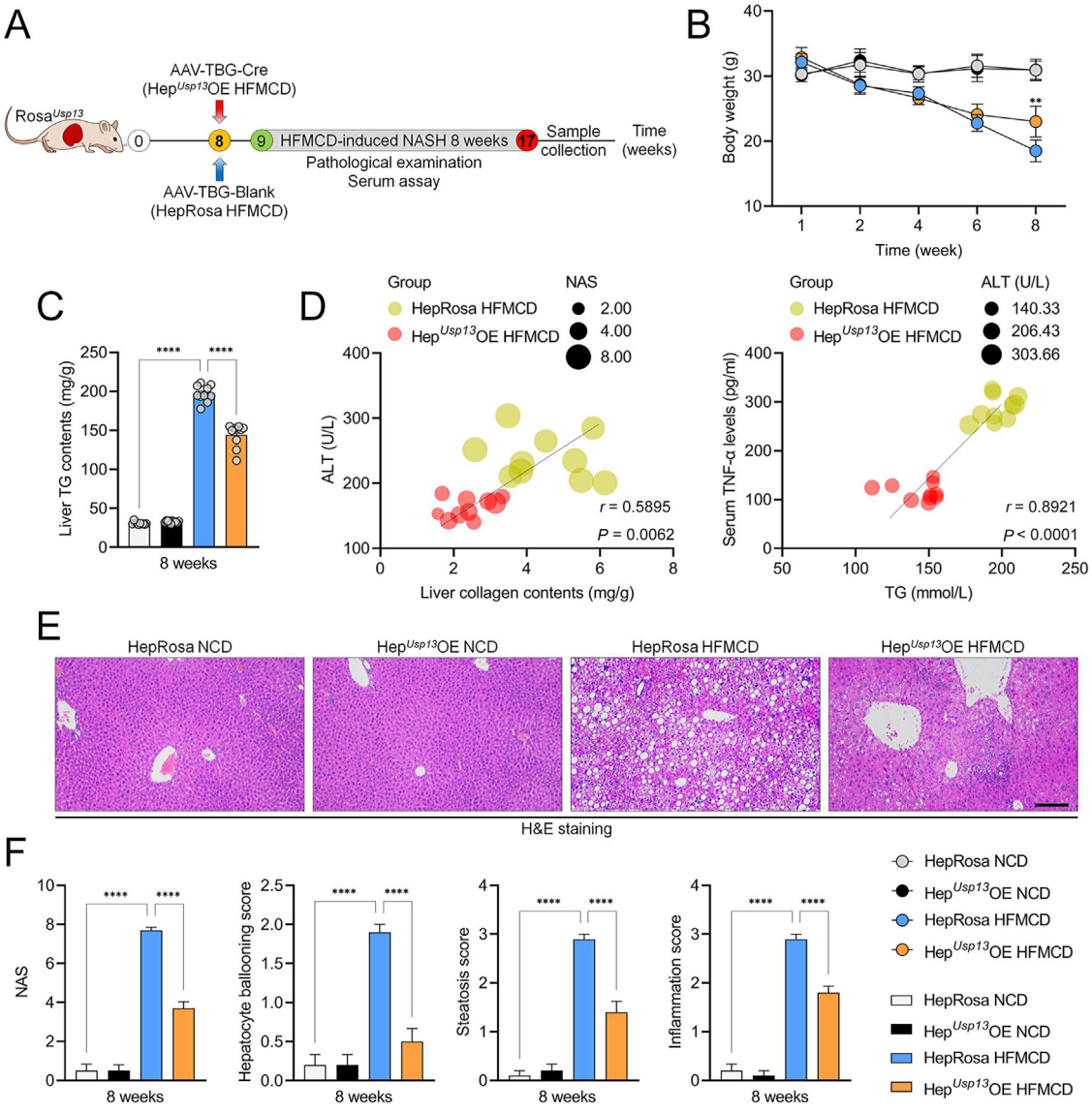

Figure 7 Forced hepatocyte USP13 activation alleviates HFMCD diet-induced NASH phenotypes. (A) Schematic diagram of AAV-TBG-Cre-mediated *Usp13* overexpression in liver of 8-weeks NCD or HFMCD diet-fed Rosa^{Usp13} mice (Hep^{Usp13}OE NCD; Hep^{Usp13}OE HFMCD). The AAV-TBG-blank was used as control (HepRosa NCD; HepRosa HFMCD). (B, C) Records for the body weight (B) and liver TG levels (C) of the Hep^{Usp13}OE HFMCD and HepRosa HFMCD mice ($n = 10$ mice per group). (D) Pearson correlation analyses indicating the correlations between ALT levels and liver collagen contents ($r = 0.5895$, $P = 0.0062$) (left), and TG levels and serum TNF-α levels ($r = 0.8921$, $P < 0.0001$) (right) in Hep^{Usp13}OE HFMCD and HepRosa HFMCD mice. $P < 0.001$ for all of these correlations ($n = 10$ per parameter; $n = 30$ in total). (E, F) Representative pictures of H&E staining (E) and histological NAS score (F) changes in Hep^{Usp13}OE HFMCD and HepRosa HFMCD mice (magnification, 100 ×; $n = 10$ images per group). Data are expressed as mean ± SEM. The relevant experiments presented in this part were performed independently at least three times. $^{**}P < 0.01$, $^{****}P < 0.0001$.

signaling cascade MAP3K7−NF-κB, MEK3/4−JNK hyperactivation. Thus, hepatocyte USP13 displays an important target for NASH treatment, clinical pharmaceutics and new drug research development.

As it is, a number of molecular targets and potential clinical application drugs for NAFLD/NASH treatment have been extensively studied[9–11]. Recently, increasing evidence revealed that IRHOM2 plays a critical role in the progression of

Flag-Irhom2. (L) Representative immunoprecipitation and immunoblotting bands showing the indicated protein in the *Usp13* KO-L02 cells transfected with HA-USP13, HA-USP13 (M664E/M739E), Flag-Irhom2 and Myc-Ubc13 vectors in response to PA treatment. (M) Representative immunoprecipitation and immunoblotting bands displaying the ubiquitination levels of Irhom2 and indicated protein expression in lysates of WT L02 cells and *Ubc13*-deletion (*Ubc13* KO) L02 cells transfected with HA-USP13, HA-USP13 (M664E/M739E), Flag-Irhom2 and Myc-Ub vectors in response to PA challenge.

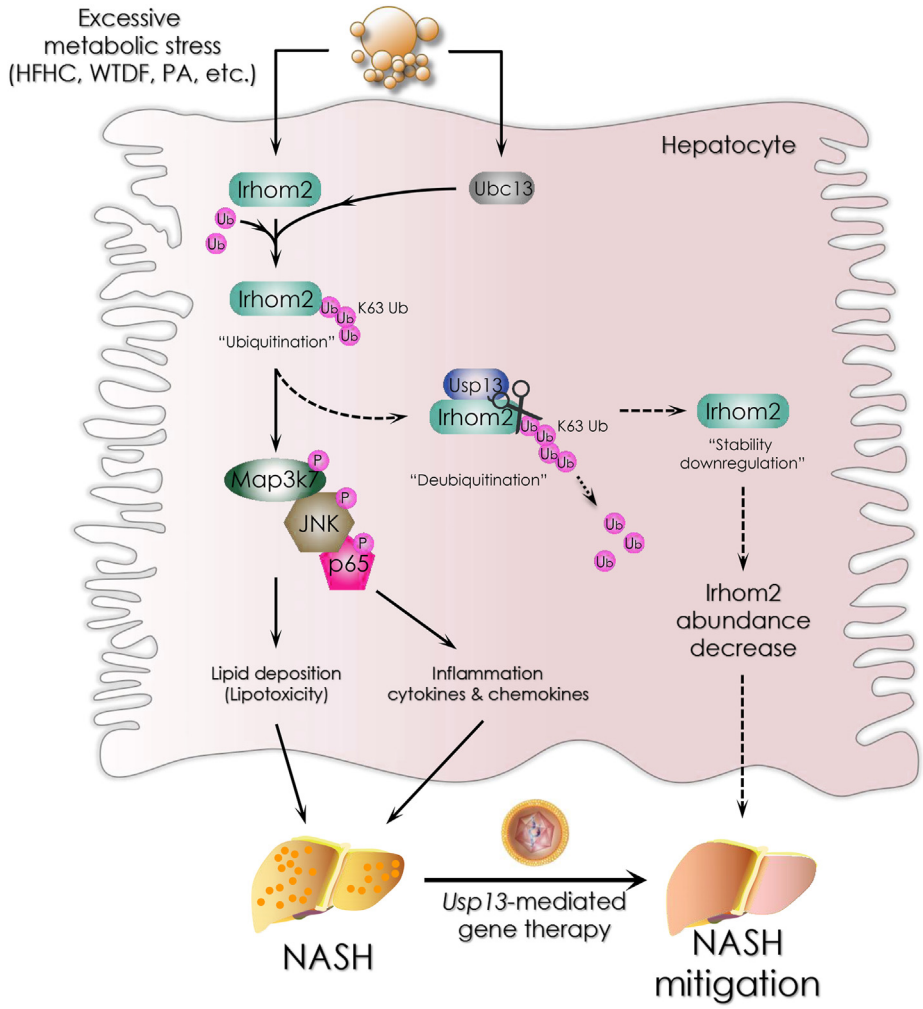

Figure 8 Schematic illustration of cellular and molecular events underlying hepatocyte USP13−Irhom2 axis-regulated nonalcoholic steatohepatitis (NASH). In response to a continuous metabolic insults, Irhom2 expression is elevated in hepatocytes, and accordingly conjugated with K63-linked polyubiquitination by Ubc13, leading to the hyperactivation of downstream Map3k7-Jnk and NF-κB p65, thus promoting inflammatory response. Forced USP13 activation in hepatocytes directly interact with Irhom2 to remove the K63 ubiquitination of Irhom2, resulting in decrease of Irhom2 stability and abundance, thereby suppressing lipid accumulation-associated hepatosteatosis and inflammation-triggered nonalcoholic steatohepatitis (NASH).

hepatosteatosis, including the regulation of liver inflammation, lipid metabolism and glucose homeostasis[12,13]. Acutely activated IRHOM2 induced by metabolism stress promotes exacerbation of metabolic profiles and elevated liver inflammation. Indeed, our previous works also confirmed that metabolic stimulation-induced increased IRHOM2 could recruit MAP3K7 to boost its phosphorylation, resulting in activation of downstream pro-inflammatory signaling cascade[12,13]. Of note, knockdown or inhibition of MAP3K7 is able to markedly mitigate NASH phenotype. However, complete ablation of *MAP3K7* in hepatocytes leads to severe hepatocyte death, inflammation, fibrosis and development of hepatocellular carcinoma (HCC); these phenotypes rely on TNF-α-associated signaling[28]. The peculiar phenomena indicate that the reduction of MAP3K7 abundance contributes to the alleviation of NASH, but it is still regulated by other potential unknown factors. Deletion of the entire MAP3K7 not only does not reduce inflammation, but also enhances possible compensatory pathways that further boost hepatocyte inflammatory necrosis and hepatofibrosis-associated HCC development. Coincidently, the maturation of the TNF-α converting enzyme (TACE), which controls release of TNF-α and its biological activity *in vivo* is tightly regulated by IRHOM2. Global *IRHOM2* deletion or hepatocyte-specific *IRHOM2* deletion significantly promotes inactivation of MAP3K7 and its signaling cascades. These findings further suggest that MAP3K7 is a downstream signal of IRHOM2, and its physiological activity changes are strictly controlled by IRHOM2. Suppression of IRHOM2 in pathogenesis may be an effective approach for NASH treatment. Although IRHOM2, a "rising star", has potential to be a target in inflammation-related diseases, there are still few studies on its regulatory mechanism. Previous studies have suspected that IRHOM2 abundance could be significantly regulated by E3 ubiquitin ligases or deubiquitinating enzymes *via* K63- or K48-linked ubiquitination[12,13]. The *in vitro* study also indicates that in response to inflammatory stimuli, UBC13, a key ubiquitin-conjugating enzyme, markedly facilitated K63-linked ubiquitination of IRHOM2. Currently, we determined, for the first time, that liver USP13 interacts with IRHOM2 and restrains its K63-linked

ubiquitination of IRHOM2 by UBC13. Thus, these results present the protective function of USP13 as an effective restrainer of IRHOM2 in response to the metabolism stresses, which could be regarded as a novel therapeutic molecule target for NASH treatment.

USP13, a key member of the deubiquitinating enzyme (DUB) superfamily with "multi-faced" function, has been confirmed as an important regulator in many cell events. Our findings suggested that USP13 activity *in vivo* and *in vitro* experiments were significantly decreased upon metabolic stresses challenge. Previous study demonstrated that USP13 has ability to suppress produce of pro-inflammatory cytokines by the deubiquitination of STING[18]. In addition, dysfunctional USP13 dramatically exacerbated chronic organ or tissue injury by increasing oxidative stress injury, inflammatory infiltration or cell apoptosis in different disease models, *e.g.*, osteoarthritis, sepsis and pulmonary bulla, *via* regulation of phosphatase and tensin homolog (PTEN), interleukin 1 receptor associated kinase 4 (IRAK4), thioredoxin interacting protein (TXNIP) or AP1 signaling[29−33]. Our results further reveal that USP13 exhibited anti-inflammatory function and regulatory features of metabolism homeostasis by blocking K63-linked IRHOM2 ubiquitination and activation of its downstream signaling pathway. Notably, the suppressive function of USP13 on IRHOM2 is mightily dependent on its activity. USP13 abundance is inversely correlated with IRHOM2 expression, increased liver inflammation, and serum concentration of lipid contents in human patients with NASH phenotype and NASH model of rodent. In the *in vivo* experiments, mice with *Usp13* deletion exhibited elevated liver injury severity. While other USP13 substrates deactivation associated with inflammation may also conduce to the proinflammatory effects we investigate with *Usp13* knockout, none of these targets is indicated to significantly promote inflammation as IRHOM2 does. Also, *Usp13* deficiency displayed increased CD11b and F4/80 positive inflammatory cells infiltration in fatty liver. Previous reports have also demonstrated that hyperactivated kupffer cells (KCs) as the main type of hepatic macrophages primarily contribute to increased inflammation levels. Since circulatory inflammation can remarkably result in the development and progression of system metabolic disorders, other activated immune cells in the blood circulation may also accelerate infiltration in the liver. At the same time, in this work, we also found that USP13 is a direct and potent interaction partner of IRHOM2. USP13 blocked IRHOM2-mediated activation of downstream signaling cascade by suppressing its K63-linked ubiquitination by UBC13 in hepatocytes. Intriguingly, the mutation of USP13 (M664E/M739E) fail to catalyze deubiquitination of IRHOM2 both *in vivo* and *in vitro*, suggesting that UBA1/2 domains determine both the IRHOM2 interaction and its downstream MAP3K7−NF-κB, MEK3/4−JNK signaling activity in the progression of NASH. Thus, these findings further indicate that the core catalytic function of UBA domains of USP13 may be a strict target for intercepting metabolic insults-driven chronic inflammation and associated metabolic disorders.

5. Conclusions

Collectively, in the present study (Fig. 8), we reveal that USP13 is a potent and novel eliminator of IRHOM2 activity in the pathological process of NASH. Liver USP13, especially the UBA1/2 domain, interacts with IRHOM2 and restrains its ubiquitination by UBC13 and subsequent downstream signaling cascade activation, resulting in mitigation of NASH pathologies. The current signaling pathway provides a possibly novel target for the NASH treatment of this world-wide disease.

Acknowledgments

This work was supported by (1) National Natural Science Foundation of China (NSFC Grant Nos. 81703527 and 82200652); (2) Chongqing Research Program of Basic Research and Frontier Technology (Grant Nos. cstc2017jcyjAX0356, cstc2018jcyjA3686, cstc2018jcyjAX0784, cstc2018jcyjA1472, cstc2018jcyjAX0811, cstc2018jcyjA3533, and KJZD-M201801601, China); (3) School-level Research Program of Chongqing University of Education (Grant Nos. KY201710B and 17GZKP01, China); (4) Advanced Programs of Post-doctor of Chongqing (Grant No. 2017LY39, China); (5) Science and Technology Research Program of Chongqing Education Commission of China (Grant Nos. KJQN201901608, KJQN201901615, KJ1601402, and KJZD-K202001603); (6) Children's Research Institute of National Center for Schooling Development Programme and Chongqing University of Education (Grant No. CSDP19FSO1108, China); (7) Chongqing Professional Talents Plan for Innovation and Entrepreneurship Demonstration Team (CQCY201903258, China).

Author contributions

Conceptualization & Methodology: Minxuan Xu, Jun Tan, Chenxu Ge, Liancai Zhu, Wei Dong, Bochu Wang; Investigation: Minxuan Xu, Jun Tan, Chenxu Ge, Liancai Zhu, Wei Dong, Xianling Dai, Qin Kuang, Shaoyu Zhong, Lili Lai, Chao Yi, Qiang Li, Deshuai Lou, Linfeng Hu, Xi Liu, Gang Kuang, Jing Luo, Jing Feng, Bochu Wang; Data analysis: Minxuan Xu, Jun Tan, Chenxu Ge, Liancai Zhu, Wei Dong; Funding acquisition, Project administration & Supervision: Minxuan Xu, Jun Tan, Wei Dong, Bochu Wang; Writing-original draft: Minxuan Xu, Jun Tan, Chenxu Ge, Liancai Zhu, Wei Dong, Bochu Wang; Writing-review & editing: Minxuan Xu, Bochu Wang, Jun Tan.

Conflicts of interest

Authors declare that they have no competing interests.

Appendix A. Supporting information

Supporting data to this article can be found online at https://doi.org/10.1016/j.apsb.2022.12.006.

References

1. Blüher M. Obesity: global epidemiology and pathogenesis. *Nat Rev Endocrinol* 2019;**15**:288−98.
2. Canfora EE, Meex RCR, Venema K, Blaak EE. Gut microbial metabolites in obesity, NAFLD and T2DM. *Nat Rev Endocrinol* 2019;**15**:261−73.
3. Friedman SL, Neuschwander-Tetri BA, Rinella M, Sanyal AJ. Mechanisms of NAFLD development and therapeutic strategies. *Nat Med* 2018;**24**:908−22.
4. Powell-Wiley TM, Poirier P, Burke LE, Després JP, Gordon-Larsen P, Lavie CJ, et al. Obesity and cardiovascular disease: a scientific statement from the American Heart Association. *Circulation* 2021;**143**:e984−1010.

5. Cai J, Zhang XJ, Li H. Progress and challenges in the prevention and control of nonalcoholic fatty liver disease. *Med Res Rev* 2019;**39**:328−48.
6. Li F, Huangyang P, Burrows M, Guo K, Riscal R, Godfrey J, et al. FBP1 loss disrupts liver metabolism and promotes tumorigenesis through a hepatic stellate cell senescence secretome. *Nat Cell Biol* 2020;**22**:728−39.
7. Pinyol R, Torrecilla S, Wang H, Montironi C, Piqué-Gili M, Torres-Martin M, et al. Molecular characterisation of hepatocellular carcinoma in patients with non-alcoholic steatohepatitis. *J Hepatol* 2021;**75**:865−78.
8. Im YR, Hunter H, de Gracia Hahn D, Duret A, Cheah Q, Dong J, et al. A systematic review of animal models of NAFLD finds high-fat, high-fructose diets most closely resemble human NAFLD. *Hepatology* 2021;**74**:1884−901.
9. Harrison SA, Wong VW, Okanoue T, Bzowej N, Vuppalanchi R, Younes Z, et al. Selonsertib for patients with bridging fibrosis or compensated cirrhosis due to NASH: results from randomized phase III STELLAR trials. *J Hepatol* 2020;**73**:26−9.
10. Marie S, Frost KL, Hau RK, Martinez-Guerreroa L, Izua MJ, Myers MC, et al. Predicting disruptions to drug pharmacokinetics and the risk of adverse drug reactions in non-alcoholic steatohepatitis patients. *Acta Pharm Sin B* 2013;**1**:1−28.
11. Chalasani N, Garcia-Tsao G, Goodman Z, Lawitz E, Abdelmalek M, Rinella M, et al. A multicenter, randomized, double-blind, PLB-controlled trial of Galectin-3 inhibitor (GR-MD-02) in patients with NASH cirrhosis and portal hypertension. *J Hepatol* 2018;**68**:S100−1.
12. Xu M, Ge C, Zhu L, Qin Y, Du C, Lou D, et al. iRhom2 promotes hepatic steatosis by activating MAP3K7-dependent pathway. *Hepatology* 2021;**73**:1346−64.
13. Xu M, Tan J, Dong W, Zou B, Teng X, Zhu L, et al. The E3 ubiquitin-protein ligase Trim31 alleviates non-alcoholic fatty liver disease by targeting Rhbdf2 in mouse hepatocytes. *Nat Commun* 2022;**13**:1052.
14. Ni R, Song G, Fu X, Song R, Li L, Pu W, et al. Reactive oxygen species-responsive dexamethasone-loaded nanoparticles for targeted treatment of rheumatoid arthritis *via* suppressing the iRhom2/TNF-α/BAFF signaling pathway. *Biomaterials* 2020;**232**:119730.
15. Chenxu G, Minxuan X, Yuting Q, Tingting G, Jinxiao L, Mingxing W, et al. iRhom2 loss alleviates renal injury in long-term PM2.5-exposed mice by suppression of inflammation and oxidative stress. *Redox Biol* 2018;**19**:147−57.
16. Zhang Y, Li Y, Yang X, Wang J, Wang R, Qian X, et al. Uev1A−Ubc13 catalyzes K63-linked ubiquitination of RHBDF2 to promote TACE maturation. *Cell Signal* 2018;**42**:155−64.
17. Dulloo I, Muliyil S, Freeman M. The molecular, cellular and pathophysiological roles of iRhom pseudoproteases. *Open Biol* 2019;**9**:190003.
18. Sun H, Zhang Q, Jing YY, Zhang M, Wang HY, Cai Z, et al. USP13 negatively regulates antiviral responses by deubiquitinating STING. *Nat Commun* 2017;**8**:15534.
19. Zhang J, Zhang P, Wei Y, Piao HL, Wang W, Maddika S, et al. Deubiquitylation and stabilization of PTEN by USP13. *Nat Cell Biol* 2013;**15**:1486−94.
20. Liu J, Xia H, Kim M, Xu L, Li Y, Zhang L, et al. Beclin1 controls the levels of p53 by regulating the deubiquitination activity of USP10 and USP13. *Cell* 2011;**147**:223−34.
21. Yeh HM, Yu CY, Yang HC, Ko SH, Liao CL, Lin YL. Ubiquitin-specific protease 13 regulates IFN signaling by stabilizing STAT1. *J Immunol* 2013;**191**:3328−36.
22. Luo WW, Li S, Li C, Lian H, Yang Q, Zhong B, et al. iRhom2 is essential for innate immunity to DNA viruses by mediating trafficking and stability of the adaptor STING. *Nat Immunol* 2016;**17**:1057−66.
23. Li Y, Luo K, Yin Y, Wu C, Deng M, Li L, et al. USP13 regulates the RAP80−BRCA1 complex dependent DNA damage response. *Nat Commun* 2017;**8**:15752.
24. Xu MX, Tan J, Ge CX, Dong W, Zhang LT, Zhu LC, et al. Tripartite motif-containing protein 31 confers protection against nonalcoholic steatohepatitis by deactivating mitogen-activated protein kinase kinase kinase 7. *Hepatology* 2023;**77**:124−43.
25. Liu D, Zhang P, Zhou J, Liao R, Che Y, Gao MM, et al. TNFAIP3 interacting protein 3 overexpression suppresses nonalcoholic steatohepatitis by blocking TAK1 activation. *Cell Metabol* 2020;**31**:726−740.e8.
26. Farrell G, Schattenberg JM, Leclercq I, Yeh MM, Goldin R, Teoh N, et al. Mouse models of nonalcoholic steatohepatitis: toward optimization of their relevance to human nonalcoholic steatohepatitis. *Hepatology* 2019;**69**:2241−57.
27. Ratziu V, Friedman SL. Why do so many NASH trials fail?. *Gastroenterology* 2020;**S0016-5085**(20):30680−6.
28. Inokuchi-Shimizu S, Park EJ, Roh YS, Yang L, Zhang B, Song J, et al. TAK1-mediated autophagy and fatty acid oxidation prevent hepatosteatosis and tumorigenesis. *J Clin Invest* 2014;**124**:3566−78.
29. Huang J, Ye Z, Wang J, Chen Q, Huang D, Liu H. USP13 mediates PTEN to ameliorate osteoarthritis by restraining oxidative stress, apoptosis and inflammation *via* AKT-dependent manner. *Biomed Pharmacother* 2021;**133**:111089.
30. Wang Z, Jiang L, Zhang D, Chen D, Wang L, Xiao D. USP13-mediated IRAK4 deubiquitination disrupts the pathological symptoms of lipopolysaccharides-induced sepsis. *Microb Infect* 2021;**23**:104867.
31. Gregory AD, Tran KC, Tamaskar AS, Wei J, Zhao J, Zhao Y. USP13 deficiency aggravates cigarette-smoke-induced alveolar space enlargement. *Cell Biochem Biophys* 2021;**79**:485−91.
32. He J, Gregory AD, Tran KC, Tamaskar AS, Wei J, Zhao J. USP13 deficiency aggravates cigarette smoke-induced alveolar space enlargement through stabilization of TXNIP. *FASEB J* 2022;**36**:R4108.
33. Yu F, Li Y, Ye Q, Miao J, Taleb SJ, Zhao Y, et al. Lipopolysaccharide reduces USP13 stability through c-Jun N-terminal kinase activation in Kupffer cells. *J Cell Physiol* 2021;**236**:4360−8.